A single dividing cell population with imbalanced fate drives oesophageal tumour growth

Julia Frede[1], Philip Greulich[2,3], Tibor Nagy[1], Benjamin D Simons[2,3,4] & Philip H Jones[1,5*]

[1] Wellcome Trust Sanger Institute, Hinxton, CB10 1SA, UK.

[2] Cavendish Laboratory, Department of Physics, University of Cambridge, J.J. Thomson Avenue, Cambridge CB3 0HE, UK.

[3] The Wellcome Trust/Cancer Research UK Gurdon Institute, University of Cambridge, Tennis Court Road, Cambridge CB2 1QN, UK.

[4] Wellcome Trust-Medical Research Council Stem Cell Institute, University of Cambridge, UK.

[5] MRC Cancer Unit, University of Cambridge, Hutchison-MRC Research Centre, Box 197, Cambridge Biomedical Campus, Cambridge, CB2 0XZ, UK.

* Corresponding Author, email pj3@sanger.ac.uk

Understanding the cellular mechanisms of tumour growth is key for designing rational anti-cancer treatment. Here we used genetic lineage tracing to quantify cell behaviour during neoplastic transformation in a model of oesophageal carcinogenesis. We found that cell behaviour was convergent across premalignant tumours, which contained a single proliferating cell population. The rate of cell division was not significantly different in the lesions and the surrounding epithelium. However, dividing tumour cells had a uniform, small bias in cell fate so that, on average, slightly more dividing than non-dividing daughter cells were generated at each round of cell division. In invasive cancers induced by $Kras^{G12D}$ expression, dividing cell fate became more strongly biased towards producing dividing over non-dividing cells in a subset of clones. These observations argue that agents that restore the balance of cell fate may prove effective in checking tumour growth, whereas those targeting proliferation may show little selectivity.

Introduction

Epithelial tumours form when the cellular homeostasis of normal tissue is locally disrupted so that cell production exceeds cell loss (**Fig. 1a**). This may result from the rate of tumour cell division being faster than that of normal cells. A second possibility is that in tumours such as squamous cell carcinomas (SCC) that consist of a mixture of dividing and non-dividing cells, the proliferating tumour cells produce a higher proportion of dividing than non-dividing daughters[1]. This bias in cell fate results in a progressive expansion in the proliferating cell population. Thirdly, the rate of cell loss may be decreased within the tumour relative to the rate of cell production. Here we set out to resolve which of these mechanisms contribute to squamous tumour growth in the oesophagus.

Further insights into the pathogenesis of oesophageal SCC, currently the 6th commonest cause of cancer death worldwide, are urgently needed as even with the most aggressive treatment the majority of patients will die from their disease[2, 3]. Oesophageal SCC is strongly associated with tobacco exposure, and may be preceded by the development of non-invasive lesions called high-grade squamous dysplasias (HGD)[4, 5]. Oesophageal carcinogenesis has been successfully recapitulated in rodents, either by exposing animals to the mutagenic DNA alkylating agent diethylnitrosamine (DEN), which is found in tobacco smoke, or by replicating some of the genomic alterations found in human SCC in transgenic mice[6-12].

Despite the availability of mouse models, quantifying the behaviour of proliferating cells within intact tumours remains challenging. One potential approach is lineage tracing, in which expression of a heritable genetic label is induced in individual proliferating cells (**Supplementary Fig. 1a-c**)[13, 14]. As the progeny of the labelled

cell proliferate and differentiate, they generate clusters of labelled cells, termed clones, as they derive from a single cell. Analysis and statistical modelling of the number of cells in cohorts of simultaneously labelled clones sampled over a prolonged time course has revealed normal cell behaviour and how it is altered by specific oncogenic driver mutations in several tissues, including the oesophageal epithelium[15, 16]. However, the application of this approach to tumours has hitherto been frustrated by extensive inter- and intra-tumoural heterogeneity, which renders the inference of cell behaviour infeasible[14].

Resolving tumour cell behaviour requires a protocol that generates highly similar lesions at a defined time point. Murine oesophageal epithelium is an ideal tissue in which to address this challenge. The normal tissue consists of layers of keratinocytes with proliferation confined to the basal layer[13]. Lineage tracing has shown that the oesophageal epithelium contains only one type of proliferating cell, termed a progenitor. The outcome of individual progenitor divisions is unpredictable, generating either two progenitors or two non-dividing, differentiating cells or one cell of each type (**Fig. 1b**). In homeostasis, the probabilities of each division outcome are balanced so that an equal number of progenitors and non-dividing cells are generated across the progenitor population. Wounding, however, drives the progenitors local to the injury to transiently produce an excess of proliferating daughters until the epithelium is repaired[13, 17]. Mutations inactivating the Notch pathway also bias fate towards proliferation, suggesting the plasticity in progenitor cell behaviour that enables wound healing is a potential vulnerability during neoplastic transformation[15, 18].

Chemical carcinogens such as DEN induce oesophageal tumours but the number of lesions and the time they take to develop varies widely between animals[6]. We drew on the widely used and well-characterised two-stage carcinogenesis protocol in the skin, speculating that following mutagen treatment with a tumour promoting agent might drive the formation of a cohort of tumours sharing a similar phenotype[19]. We noted that side effects of the multikinase inhibitor Sorafenib include induction of SCC of the skin and head and neck in patients treated for liver, kidney and thyroid cancers[20-22]. This motivated us to test whether Sorafenib could promote oesophageal tumour formation in DEN treated mice.

Here we report that the combination of DEN followed by Sorafenib was effective at inducing cohorts of tumours that are sufficiently similar to permit the quantification of cell dynamics using transgenic cell proliferation and lineage tracing assays. We resolved cell behaviour in promoter treated epithelium, HGD and SCC. The data argues that tumours contain a single proliferating cell population whose behaviour is only subtly perturbed from that of normal progenitors.

Results

Sorafenib promotes the formation of high grade dysplasias

We set out to determine if Sorafenib could promote squamous carcinogenesis in the oesophagus, beginning by investigating the effect of treatment with Sorafenib alone. 10 days of dosing induced a marked dose-dependent increase in proliferation marker expression (**Fig. 1c,d**, **Supplementary Fig. 2a-c**). Treatment for 28 days at a 50mg/Kg dose resulted in decreased phosphorylation of ERK and AKT (**Fig. 1e-g**,

Supplementary Fig. 2d-f). However, tissue integrity was preserved and no tumours developed (**Supplementary Fig. 2g, Supplementary Table 1**), even when the duration of treatment was extended to 56 days. Apoptosis was negligible (**Supplementary Fig. 2h**). Hence, Sorafenib on its own, increased proliferation but was not tumourigenic.

Next we studied the combination of Sorafenib and the mutagen DEN. Mice were administered Sorafenib or vehicle control for 28 days after 56 days of exposure to DEN (**Fig. 2a**). The combination of DEN and Sorafenib generated an average of 3 macroscopic tumours per animal with histological features of HGD (loss of normal differentiation, nuclear atypia and loss of cell polarity extending through the entire thickness of the epithelium) (**Fig. 2b-e, Supplementary Table 1**)[4]. In contrast, animals treated with DEN and vehicle developed small areas of focal hyperplastic epithelium at a frequency of less than one lesion per mouse (**Fig. 2d,e, Supplementary Table 1**).

We next characterised the DEN/Sorafenib induced HGD further. Consistent with the disruption of terminal differentiation seen histologically, we observed a loss of expression of the cornified envelope precursor proteins LOR and FLG in lesions by immunostaining (**Fig. 2f, Supplementary Fig. 3a**). Expression of KRT14, confined to the basal layer in normal epithelium, was widespread, and KRT4, normally detected in the first suprabasal layer was only seen in and above the 3rd and 4th suprabasal cell layers (**Fig. 2f)**. We also observed increased expression of the keratinocyte stress induced proteins KRT6, induced in squamous tumours in humans and mice and KRT17, a regulator of tumour associated transcription (**Fig. 2g,**

Supplementary Fig. 3b)[23-25]. We detected apoptosis in only 0.08 +/- 0.05% (mean+/- s.e.m.) of cells (**Supplementary Fig. 2h**).

The dysplastic cells did not breach the basement membrane but protruded into the underlying submucosa (**Fig. 2h**). 3D confocal imaging revealed substantial stromal remodelling beneath the lesions. There was marked angiogenesis and lymphangiogenesis with a leukocytic infiltrate including CD11b and CD3 positive cells closely associated with the deep margin of HGD, features also seen in murine and human squamous dysplasia and SCC (**Fig. 2i-k**, **Supplementary Fig. 3c**)[26-30]. We concluded that Sorafenib promotes tumour formation in DEN treated epithelium.

We next investigated whether the common histological phenotype of the lesions was reflected at a transcriptional level. Whereas the transcriptomes of HGDs and normal adjacent epithelium differed markedly, there was comparatively little variation between HGDs (**Fig. 3a**). Gene ontology categories that were significantly different between normal epithelium and HGD included keratinocyte differentiation and inflammation associated transcripts, consistent with our findings above (**Supplementary Tables 2, 3)**. Transcripts of genes involved in RNA splicing, a process dysregulated in epidermal carcinogenesis, were also differentially expressed (**Fig. 3b**)[31]. We validated the relative expression of selected mRNAs in epithelium and HGDs by quantitative RT-PCR, observing marked upregulation of cytoskeletal associated transcripts (**Fig. 3c**).

Clonal origin of HGD lesions

Malignant transformation is thought to be a process in which lesions originate from the progeny of a single cell that progressively acquires multiple oncogenic genomic alterations[32, 33]. However, dysplastic lesions in several mouse and human tissues have

been shown to be polyclonal[34-39]. We therefore investigated the clonal origin of the HGD lesions by genetic lineage tracing. We induced a heritable genetic marking with the confetti allele, which labels cells with one of four different fluorescent proteins (**Supplementary Fig. 1a,b**) [40]. Reporter expression was induced in individual basal cells by transient expression of *cre* recombinase-mutant oestrogen receptor fusion protein (cre^{ERT}) from a xenobiotic inducible *Cyp1a1* (*Ah*) promoter following injection of low dose β-napthoflavone and tamoxifen in $Ahcre^{ERT}Rosa26^{flConfetti/wt}$ mice[41]. Animals were then treated with DEN and Sorafenib and epithelial wholemounts of HGD lesions imaged (**Fig. 3d**). If lesions arose from the clonal progeny of a single cell, they would be either unlabelled or completely labelled with a single colour. If, however, HGD derived from multiple cells, variegated labelling with multiple different coloured clones would be seen. We observed a mean of 2.7 clones (range 1-6) in 9 labelled lesions, which ranged widely in size (n=5 animals) (**Fig. 3e-g**). Similar results were obtained when the experiment was repeated with a single colour labelling system in $Ahcre^{ERT}Rosa26^{flYFP/wt}$ mice, in which cells are labelled with a yellow fluorescent protein (YFP) reporter (**Supplementary Fig. 1c, Supplementary Fig. 3d-g**)[13]. We conclude that HGD have multiple cells of origin.

$Kras^{G12D}$ expression in combination with DEN/Sorafenib treatment results in invasive squamous cell carcinomas

We speculated that altering the protocol might generate invasive SCC rather than HGD. We noted that mutations, amplifications or overexpression of growth factor receptor tyrosine kinases and genes in their downstream signalling pathways, including KRAS, are present in the majority of human oesophageal SCCs[42-44]. Furthermore, oncogenic KRAS mutations are frequent in cutaneous SCCs in patients

treated with Sorafenib[45]. These observations led us to investigate the effects of inducing the oncogenic $Kras^{G12D}$ mutant in oesophageal epithelium after DEN exposure and prior to treatment with Sorafenib (**Supplementary Fig. 1d)**[46]. This protocol resulted in lethal, invasive SCCs in 11/14 animals (**Fig. 4a-d, Supplementary Table 1**). We observed increased phospho-Erk levels in the carcinomas, consistent with Kras activation in the lesions (**Fig. 4e**). Consistent with our findings in dysplasias, KRT14 stained positive throughout the tumours, while expression of terminal differentiation marker LOR was abrogated (**Supplementary Fig. 4a,b**). The carcinomas shared a similar transcriptome (**Fig. 4f**). Among the differences in transcription between HGD and SCC were significant induction of the inflammation associated mRNAs *Ifngr2* and *Fcer1g* and changes consistent with *Kras* activation in SCC (**Fig. 4g,h**, **Supplementary Fig. 4c**). A limitation of inducing SCC with this protocol is that we were unable to use lineage tracing to determine whether the tumours were monoclonal or polyclonal in origin.

Proliferating cell dynamics in Sorafenib treated epithelium

The data above show that the combination of DEN and Sorafenib was effective in inducing HGD and SCC that shared similar features. We therefore set out to quantify how proliferating cell behaviour changed in promoter treated epithelium, HGD and SCC.

We began by analysing the effect of Sorafenib treatment by using the dilution of a transiently expressed transgenic histone-green fluorescent protein (HGFP) to infer the mean rate of epithelial cell division[13, 47, 48]. Transgenic animals were treated with doxycycline (dox) to induce HGFP transcription from a synthetic dox-regulated promoter, resulting in high level expression of HGFP throughout the epithelium

(**Supplementary Fig. 1e**)[49, 50]. Following withdrawal of dox, HGFP levels were measured by confocal imaging of epithelial wholemounts. Histone mRNA is short lived, so HGFP message is unlikely to persist following dox withdrawal and the cessation of transcription[51, 52]. Assuming that the rate of HGFP protein degradation is small compared with the cell cycle time, the rate of HGFP decrease will reflect the rate at which it is diluted by cell division (**Fig. 5a-c**, **Supplementary Table 4**). Analysis of HGFP levels indicated the mean cell division rate rose from once every 3.5 days in controls to a rate of once a day during Sorafenib treatment (**Supplementary Fig. 5a,b, Supplementary Note 2.1**) .

To address how the fate of individual progenitor cells was perturbed by treatment with Sorafenib, we used lineage tracing, inducing sparse genetic labelling with YFP to yield well-separated clones in $Ahcre^{ERT}Rosa26^{flYFP/wt}$ mice during a course of Sorafenib treatment (**Fig. 5d**)[13]. 12 days after clonal induction, animals were sacrificed, and multicellular YFP expressing clones (233 from 3 animals) imaged (**Fig. 5d-f, Supplementary Fig. 5c-f, Supplementary Table 4**). To assess whether the clone size data could be accommodated within the cell fate paradigm of normal OE (**Fig. 5g**), we implemented cell fate rules in a stochastic model, which was simulated for a wide range of parameters (**Supplementary Note 1.2.2**). Taking the cell cycle times determined by HGFP dilution as a prior, we found the best match of model and data using Bayesian inference (**Fig. 5f**). This confirmed that the data complies with the same paradigm as normal epithelium, but with a marked increase in both the proportion of divisions leading to asymmetric fate and the rate of cell stratification, in line with the increased cell division rate (**Fig. 5f,g, Supplementary Table 5, Supplementary Note 2.2**). We subsequently repeated the experiment analysing clones in Sorafenib treated epithelium 21 days after induction. The

observed clone size distribution at 21 days accurately matched the predicted clone size distribution based on the parameter estimates from the 12 day experiment, confirming our cell fate model (**Supplementary Fig. 5g-j, Supplementary Table 4**). We further tested the predictions of the lineage tracing analysis by independent assays, which were consistent with model predications (**Methods, Supplementary Fig. 5k-q, Supplementary Note 2.2**). We concluded that Sorafenib established a new 'steady-state' with a faster rate of cell turnover than control tissue, sustained by the same single dividing cell population that maintains the normal epithelium.

Cell dynamics in dysplasia

Next we investigated proliferating cell behaviour within HGD lesions. To map the location of proliferating cells, animals were injected with EdU (**Fig. 6a**)[53]. After 24 hours, the vast majority of EdU+ cells were found at the edge of lesions (**Fig. 6b**). However, 5 days later, residual EdU+ cells were found in the centre of the lesion, arguing non-dividing cells migrate from the proliferative rim to the core of the lesion where they accumulate (**Fig. 6c**). This was confirmed by HGFP dilution assay, which showed that cells retaining detectable levels of HGFP remained in the centre of the lesions for at least 38 days after dox withdrawal, but were absent elsewhere in the tissue (**Fig. 6d,e**). We concluded that HGD were characterised by a centripetal migration of cells from the proliferative margin to the non-dividing centre, a phenomenon also reported in human squamous tumours[1]. A possible explanation for the retention of non-dividing cells is that the disrupted expression of proteins required for late terminal differentiation reduces the rate of shedding of dysplastic cells from the surface of the lesion in comparison with normally differentiated cells in the adjacent epithelium (**Fig. 2f, Supplementary Fig. 3a**).

Next we estimated the rate of cell division in HGD and the adjacent epithelium (**Fig. 6f-i, Supplementary Fig. 6a-d, Supplementary Table 4**). Analysis of HGFP dilution showed the mean cell division rate was once per day both in the lesion and the surrounding epithelium, assuming the stability of HGFP is not altered by neoplastic transformation (**Fig. 6h,i, Supplementary Fig. 6d**, **Supplementary Table 5, Supplementary Note 2.1**). To track the fate of individual cells in HGD, we performed lineage tracing in YFP reporter mice, imaging clones within wholemounts at 13 and 22 days post-induction (**Fig. 7a-c, Supplementary Fig. 6e,f, Supplementary Table 4)**. The clone size distribution remained unimodal, consistent with dividing cells belonging to a single progenitor population following a defined stochastic fate. We therefore sought the simplest modification of normal cell dynamics that could accommodate the observed clone sizes, in the form of a constant statistical bias in cell fate towards the production of proliferating cells. We thus simulated the original model relaxing the previous restriction on equal cell fate ratios, and tested this model on the clone size distributions through Bayesian inference (**Fig. 1b**, **Supplementary Note 2.3**). This showed an excellent agreement between experiment and theory and gave a bias of around 4% towards divisions producing two cycling over two non-dividing cells (**Fig. 7c,d, Supplementary Table 5, Supplementary Note 2.3**). The rate of cell loss was also reduced (**Fig. 7d, Supplementary Table 5, Supplementary Note 2.3**). This is consistent with both the observed disruption of the differentiation process that occurs prior to cell shedding from the epithelial surface and the accumulation of non-dividing cells in the lesion core (**Fig. 2f, Supplementary Fig. 3a, Fig. 6c,e).** Analysis of the clone size distribution in the surrounding epithelium indicated the cell dynamics were not significantly different from those of epithelium in mice treated with Sorafenib alone,

suggesting that the effects of the combination of DEN and Sorafenib treatment on cell behaviour are confined to the HGD lesions (**Supplementary Fig. 6g**). To further validate the analysis, we repeated the experiment in mice carrying the confetti reporter allele, which allows labelling with four different colours, thereby reducing the probability that clones with the same colour merge to create a misleadingly large apparent 'clone' (**Fig. 7e-g, Supplementary Note 2.3**). We obtained similar results to YFP for all parameters but the loss rate, which was increased in the confetti experiment. This discrepancy may be attributed to the higher sensitivity of detection of labelled cells in the single colour assay, in which immunostaining was used to visualise YFP expression (see **Methods**). We concluded that a *single* proliferating cell population with a small constant cell fate bias towards the production of dividing cells is responsible for the growth of the dysplastic lesions (**Fig. 7d**).

This analysis made the counterintuitive prediction that the proportion of dividing cells amongst the total cell population should be *decreased* within HGD compared with the surrounding epithelium, as the decreased rate of cell loss in HGD would result in the accumulation of non-dividing cells. The proportion of cells expressing the proliferation associated antigen Ki67 was indeed reduced within HGD (**Fig. 7h**).

Cell dynamics in squamous cell carcinoma

Finally, we investigated proliferating cell behaviour in SCC. We performed lineage tracing in triply transgenic Ahcre^{ERT}Rosa26$^{flYFP/wt}$Kras$^{flG12D/wt}$ animals, induced after DEN exposure and prior to Sorafenib treatment (**Fig. 8a-h, Supplementary Fig. 7a-d, Supplementary Table 4**). The YFP allele was less efficiently recombined than the Kras^{G12D} allele, resulting in sparse labelling in tumours. In these experiments, the clones reflect the fate of labelled cells and their progeny from when they were

labelled in normal appearing epithelium at the end of DEN treatment until they are sampled within SCC. We observed that 26/31 SCC contained an average of 5 (range 1-20) YFP positive clones (**Fig. 8e**). Two thirds of the clones had a size distribution quantitatively consistent with the cell dynamics seen in HGD (**Fig. 8b,f,g, Supplementary Fig. 7c, Supplementary Note 2.4**). The sizes of the vast majority of the remaining clones could be captured within the same model paradigm, but with a larger bias towards proliferating cell fate (**Fig. 8c,h, Supplementary Fig. 7d, Supplementary Note 2.4**). Only 2% of clones expanded significantly faster than the model prediction (**Fig. 8d,f**), suggesting that the same paradigm of progenitor dynamics applies to almost all clones in SCC, but with a variable bias in cell fate (**Fig. 8i**). Strikingly, as with HGD, the proportion of Ki67 positive cells was lower in SCC than in the surrounding normal epithelium (**Fig. 8j, Supplementary Fig. 7e**).

Conclusion

In summary, the DEN/Sorafenib carcinogenesis protocol generates multiple, synchronous and phenotypically similar oesophageal HGDs. Additional expression of an oncogenic Ras allele generates invasive SCC. These tumours are sufficiently similar to allow the quantitative resolution of cell dynamics and offer a model of carcinogenesis that can be combined with transgenic tools to explore many other aspects of tumour biology.

Linage tracing reveals that cells in dysplasias share a common dynamics despite their polyclonal origin. It remains to be resolved whether a single clone recruits surrounding cells or whether multiple clones collaborate in establishing a lesion.

Within oesophageal tumours, we show that dividing cells are a single population with a bias towards the production of dividing over non dividing daughter cells and no

significant change in the rate of cell division (**Supplementary Fig. 7f).** In dysplasia cell behaviour is remarkably uniform with a small constant fate bias. In contrast, early carcinoma is characterised by the emergence of a sub-set of clones with an increased bias towards proliferation that compete for dominance within the tumour[33, 54].

Our results also argue that the 'cancer stem cell' hypothesis, which proposes that tumour expansion depends on a hierarchy of proliferating cells, does not apply to squamous neoplasia in mice[55, 56]. We conclude that targeting imbalanced cell fate may provide an attractive strategy to arrest tumour progression.

Acknowledgements

We thank Dr Shalini Malhotra, Consultant Upper GI Pathologist at Addenbrookes Hospital Cambridge for assistance with histopathology. This work was funded by a Cancer Research UK Programme Grant (C609/A17257) to P.H.J, a Medical Research Council Grant-in-Aid and core support at the Wellcome Trust Sanger Institute. P.G. was funded by a DFG Research Fellowship and EPSRC Critical Mass Grant. B.D.S. acknowledges the support of the Wellcome Trust (grant number 098357/Z/12/Z) and the core funding to the Gurdon Institute by the Wellcome Trust and Cancer Research UK.

Author Contributions

JF designed and performed experiments, analysed data and wrote the manuscript, PG analysed data and wrote the manuscript, BDS analysed data and wrote the manuscript, PHJ initiated and supervised the project and wrote the manuscript.

References:

1. Pierce, G.B. & Wallace, C. Differentiation of Malignant to Benign Cells. *Cancer Research* **31**, 127-134 (1971).
2. Torre, L.A. *et al.* Global cancer statistics, 2012. *CA: A Cancer Journal for Clinicians* **65**, 87-108 (2015).
3. Shapiro, J. *et al.* Neoadjuvant chemoradiotherapy plus surgery versus surgery alone for oesophageal or junctional cancer (CROSS): long-term results of a randomised controlled trial. *The Lancet. Oncology* **16**, 1090-1098 (2015).
4. Taylor, P.R., Abnet, C.C. & Dawsey, S.M. Squamous dysplasia – the precursor lesion for esophageal squamous cell carcinoma. *Cancer epidemiology, biomarkers & prevention : a publication of the American Association for Cancer Research, cosponsored by the American Society of Preventive Oncology* **22**, 540-552 (2013).
5. Wang, G.Q. *et al.* Histological precursors of oesophageal squamous cell carcinoma: results from a 13 year prospective follow up study in a high risk population. *Gut* **54**, 187-192 (2005).
6. Rubio, C.A., Liu, F.S., Chejfec, G. & Sveander, M. The induction of esophageal tumors in mice: dose and time dependency. *In Vivo* **1**, 35-38 (1987).
7. Hecht, S.S. Tobacco smoke carcinogens and lung cancer. *Journal of the National Cancer Institute* **91**, 1194-1210 (1999).
8. Reuber, M.D. Histopathology of preneoplastic and neoplastic lesions of the esophagus in BUF rats ingesting diethylnitrosamine. *Journal of the National Cancer Institute* **58**, 313-321 (1977).
9. Liu, K. *et al.* Sox2 cooperates with inflammation-mediated Stat3 activation in the malignant transformation of foregut basal progenitor cells. *Cell Stem Cell* **12**, 304-315 (2013).
10. Stairs, D.B. *et al.* Deletion of p120-catenin results in a tumor microenvironment with inflammation and cancer that establishes it as a tumor suppressor gene. *Cancer Cell* **19**, 470-483 (2011).
11. Opitz, O.G. *et al.* A mouse model of human oral-esophageal cancer. *J Clin Invest* **110**, 761-769 (2002).
12. Ohkoshi, A., Suzuki, T., Ono, M., Kobayashi, T. & Yamamoto, M. Roles of Keap1-Nrf2 System in Upper Aerodigestive Tract Carcinogenesis. *Cancer Prev Res (Phila)* (2012).
13. Doupe, D.P. *et al.* A single progenitor population switches behavior to maintain and repair esophageal epithelium. *Science* **337**, 1091-1093 (2012).
14. Alcolea, M.P. & Jones, P.H. Tracking cells in their native habitat: lineage tracing in epithelial neoplasia. *Nat Rev Cancer* **13**, 161-171 (2013).
15. Alcolea, M.P. *et al.* Differentiation imbalance in single oesophageal progenitor cells causes clonal immortalization and field change. *Nat Cell Biol* **16**, 615-622 (2014).
16. Vermeulen, L. *et al.* Defining stem cell dynamics in models of intestinal tumor initiation. *Science* **342**, 995-998 (2013).
17. Roshan, A. *et al.* Human keratinocytes have two interconvertible modes of proliferation. *Nat Cell Biol* **18**, 145-156 (2016).
18. Alcolea, M.P. & Jones, P.H. Cell competition: Winning out by losing notch. *Cell Cycle* **14**, 9-17 (2015).

19. Abel, E.L., Angel, J.M., Kiguchi, K. & DiGiovanni, J. Multi-stage chemical carcinogenesis in mouse skin: Fundamentals and applications. *Nature protocols* **4**, 1350-1362 (2009).
20. Wilhelm, S.M. *et al.* Preclinical overview of sorafenib, a multikinase inhibitor that targets both Raf and VEGF and PDGF receptor tyrosine kinase signaling. *Mol Cancer Ther* **7**, 3129-3140 (2008).
21. Arnault, J.P. *et al.* Keratoacanthomas and squamous cell carcinomas in patients receiving sorafenib. *J Clin Oncol* **27**, e59-61 (2009).
22. Schneider, T.C. *et al.* (Secondary) solid tumors in thyroid cancer patients treated with the multi-kinase inhibitor sorafenib may present diagnostic challenges. *BMC Cancer* **16**, 31 (2016).
23. Takahashi, K. & Coulombe, P.A. Defining a region of the human keratin 6a gene that confers inducible expression in stratified epithelia of transgenic mice. *J Biol Chem* **272**, 11979-11985 (1997).
24. Wilson, J.B., Weinberg, W., Johnson, R., Yuspa, S. & Levine, A.J. Expression of the BNLF-1 oncogene of Epstein-Barr virus in the skin of transgenic mice induces hyperplasia and aberrant expression of keratin 6. *Cell* **61**, 1315-1327 (1990).
25. Hobbs, R.P. *et al.* Keratin-dependent regulation of Aire and gene expression in skin tumor keratinocytes. *Nat Genet* **47**, 933-938 (2015).
26. Hanahan, D. & Folkman, J. Patterns and Emerging Mechanisms of the Angiogenic Switch during Tumorigenesis. *Cell* **86**, 353-364 (1996).
27. Schoppmann, S.F. *et al.* Lymphangiogenesis and lymphovascular invasion diminishes prognosis in esophageal cancer. *Surgery* **153**, 526-534 (2013).
28. Kubota, Y. *et al.* The onset of angiogenesis in a multistep process of esophageal squamous cell carcinoma. *Front Biosci (Landmark Ed)* **14**, 3872-3878 (2009).
29. Zheng, W., Aspelund, A. & Alitalo, K. Lymphangiogenic factors, mechanisms, and applications. *The Journal of Clinical Investigation* **124**, 878-887 (2014).
30. Kitadai, Y. *et al.* Clinicopathological significance of vascular endothelial growth factor (VEGF)-C in human esophageal squamous cell carcinomas. *International Journal of Cancer* **93**, 662-666 (2001).
31. Jensen, M.A., Wilkinson, J.E. & Krainer, A.R. Splicing factor SRSF6 promotes hyperplasia of sensitized skin. *Nat Struct Mol Biol* **21**, 189-197 (2014).
32. Nowell, P.C. The clonal evolution of tumor cell populations. *Science* **194**, 23-28 (1976).
33. Martincorena, I. & Campbell, P.J. Somatic mutation in cancer and normal cells. *Science* **349**, 1483-1489 (2015).
34. Winton, D.J., Blount, M.A. & Ponder, B.A. Polyclonal origin of mouse skin papillomas. *Br J Cancer* **60**, 59-63 (1989).
35. Ross-Innes, C.S. *et al.* Whole-genome sequencing provides new insights into the clonal architecture of Barrett's esophagus and esophageal adenocarcinoma. *Nat Genet* **47**, 1038-1046 (2015).
36. Parsons, B.L. Many different tumor types have polyclonal tumor origin: Evidence and implications. *Mutation Research/Reviews in Mutation Research* **659**, 232-247 (2008).
37. Schepers, A.G. *et al.* Lineage Tracing Reveals Lgr5+ Stem Cell Activity in Mouse Intestinal Adenomas. *Science* **337**, 730-735 (2012).

38. Maddipati, R. & Stanger, B.Z. Pancreatic Cancer Metastases Harbor Evidence of Polyclonality. *Cancer Discov* **5**, 1086-1097 (2015).
39. Shin, K. *et al.* Cellular origin of bladder neoplasia and tissue dynamics of its progression to invasive carcinoma. *Nat Cell Biol* **16**, 469-478 (2014).
40. Snippert, H.J. *et al.* Intestinal crypt homeostasis results from neutral competition between symmetrically dividing Lgr5 stem cells. *Cell* **143**, 134-144 (2010).
41. Kemp, R. *et al.* Elimination of background recombination: somatic induction of Cre by combined transcriptional regulation and hormone binding affinity. *Nucleic Acids Res* **32**, e92 (2004).
42. Gao, Y.B. *et al.* Genetic landscape of esophageal squamous cell carcinoma. *Nat Genet* (2014).
43. Song, Y. *et al.* Identification of genomic alterations in oesophageal squamous cell cancer. *Nature* **509**, 91-95 (2014).
44. Lin, D.C. *et al.* Genomic and molecular characterization of esophageal squamous cell carcinoma. *Nat Genet* **46**, 467-473 (2014).
45. Arnault, J.P. *et al.* Skin tumors induced by sorafenib; paradoxic RAS-RAF pathway activation and oncogenic mutations of HRAS, TP53, and TGFBR1. *Clin Cancer Res* **18**, 263-272 (2012).
46. Jackson, E.L. *et al.* Analysis of lung tumor initiation and progression using conditional expression of oncogenic K-ras. *Genes Dev* **15**, 3243-3248 (2001).
47. Wilson, A. *et al.* Hematopoietic stem cells reversibly switch from dormancy to self-renewal during homeostasis and repair. *Cell* **135**, 1118-1129 (2008).
48. Mascre, G. *et al.* Distinct contribution of stem and progenitor cells to epidermal maintenance. *Nature* **489**, 257-262 (2012).
49. Tumbar, T. *et al.* Defining the epithelial stem cell niche in skin. *Science* **303**, 359-363 (2004).
50. Hochedlinger, K., Yamada, Y., Beard, C. & Jaenisch, R. Ectopic expression of Oct-4 blocks progenitor-cell differentiation and causes dysplasia in epithelial tissues. *Cell* **121**, 465-477 (2005).
51. Harris, M.E. *et al.* Regulation of histone mRNA in the unperturbed cell cycle: evidence suggesting control at two posttranscriptional steps. *Mol Cell Biol* **11**, 2416-2424 (1991).
52. Whitfield, M.L. *et al.* Stem-loop binding protein, the protein that binds the 3' end of histone mRNA, is cell cycle regulated by both translational and posttranslational mechanisms. *Mol Cell Biol* **20**, 4188-4198 (2000).
53. Salic, A. & Mitchison, T.J. A chemical method for fast and sensitive detection of DNA synthesis in vivo. *Proc Natl Acad Sci U S A* **105**, 2415-2420 (2008).
54. Tabassum, D.P. & Polyak, K. Tumorigenesis: it takes a village. *Nat Rev Cancer* **15**, 473-483 (2015).
55. Kreso, A. & Dick, J.E. Evolution of the cancer stem cell model. *Cell Stem Cell* **14**, 275-291 (2014).
56. Meacham, C.E. & Morrison, S.J. Tumour heterogeneity and cancer cell plasticity. *Nature* **501**, 328-337 (2013).
57. Clayton, E. *et al.* A single type of progenitor cell maintains normal epidermis. *Nature* **446**, 185-189 (2007).
58. Doupe, D.P., Klein, A.M., Simons, B.D. & Jones, P.H. The ordered architecture of murine ear epidermis is maintained by progenitor cells with random fate. *Dev Cell* **18**, 317-323 (2010).

59. Sharma, A. *et al.* Mutant V599EB-Raf regulates growth and vascular development of malignant melanoma tumors. *Cancer Res* **65**, 2412-2421 (2005).
60. Peyre, E. *et al.* A lateral belt of cortical LGN and NuMA guides mitotic spindle movements and planar division in neuroepithelial cells. *J Cell Biol* **193**, 141-154 (2011).
61. Du, P., Kibbe, W.A. & Lin, S.M. lumi: a pipeline for processing Illumina microarray. *Bioinformatics* **24**, 1547-1548 (2008).
62. Ritchie, M.E. *et al.* limma powers differential expression analyses for RNA-sequencing and microarray studies. *Nucleic Acids Res* **43**, e47 (2015).
63. Falcon, S. & Gentleman, R. Using GOstats to test gene lists for GO term association. *Bioinformatics* **23**, 257-258 (2007).
64. Szklarczyk, D. *et al.* STRING v10: protein–protein interaction networks, integrated over the tree of life. *Nucleic Acids Research* (2014).

Figure Legends

Figure 1 Cell dynamics in oesophageal squamous carcinogenesis. (**a**) Normal oesophageal epithelium is maintained by a single population of progenitor cells that divide to generate dividing (pink) and post mitotic cells (white), which exit the basal layer. In homeostatic epithelium cell production (green arrow) balances cell loss (red arrow) as proliferating cells generate equal proportions of dividing and non-dividing cells on average. In tumours, an excess of cells is generated locally through one or more of: faster cell division, indicated by the clock, an imbalance in cell fate with a bias towards producing proliferating over non-dividing progeny, Δ, or a decrease in the rate of cell loss relative to the rate of cell production. (**b**) The outcome of individual progenitor divisions is unpredictable, generating two dividing progenitors or two non-dividing, differentiating cells in symmetric divisions or one cell of each type with the probabilities shown; r is the probability of a symmetric division outcome. In homeostasis, on average equal proportions of dividing and non-dividing cells are generated. During wound healing, local progenitor cells transiently generate an excess of dividing cells until the epithelium is repaired. The probability of generating two dividing cells is increased by Δ, a measure of cell fate bias towards producing proliferating over non-dividing progeny. (**c,d**) Proliferation in Sorafenib treated oesophageal epithelium. (**c**) Protocol. Animals were given Sorafenib or vehicle only (Control) for 10 days and injected with EdU (purple arrow) 1 hour before being culled. (**d**) Confocal z stacks showing 'top down' views of typical epithelial wholemounts, representative of 3 animals per group; stained for Ki67 (green), EdU (magenta), 40,6-diamidino-2-phenylindole (DAPI, blue). Scale bar, 50 μm. (**e-g**) Effect of Sorafenib on ERK phosphorylation. (**e**) Protocol. (**f**) Representative confocal images of epithelial cryosections stained for P-ERK (Thr202/Tyr204, green),

basal marker ITGA6 (white) and DAPI (blue). Scale bar, 50 μm. Arrow, cells positive for P-ERK. Image is representative of sections from 3 animals/group. (**g**) Mean percentage of basal cells staining positive for P-ERK, (* p=0.026 by t test, n=3 animals/group). See **Supplementary Table 4** for source data for **g**.

Figure 2: Characterisation of dysplastic lesions

(**a**) Protocol. Animals were treated with DEN for 8 weeks followed by vehicle control or Sorafenib for 4 weeks. (**b**) Representative epithelial wholemount with lesions (arrows) following DEN and Sorafenib treatment. Scale bar, 1 mm. (**c**) Haematoxylin & eosin stained section of a typical high grade dysplastic lesion, arrow indicates parakeratosis. Scale bar, 100 μm. Image representative of 8 lesions. (**d,e**) Number of lesions per animal (**d**) and lesion area (**e**) in DEN and vehicle (DEN+V) and DEN and Sorafenib (DEN+S) treated animals. **p=0.003 by t-test, n=12 per group. ***p=0.0001 by Mann-Whitney test, n=28 lesions for DEN+S and 15 lesions for DEN+V group. (**f**) Differentiation within lesions. Confocal image of cyrosection from lesion stained for a terminal differentiation marker, the cornified envelope precursor protein LOR (green), KRT4 (magenta) and basal cell marker KRT14 (white). Scale bar, 200 μm. (**g**) Expression of keratinocyte stress induced protein KRT6. Confocal image of cryosection stained for KRT6 (green) and basal cell marker ITGA6 (white). Scale bar, 200 μm. Images **f,g** are typical examples of 3 lesions. (**h-k)** Stromal changes beneath HGD lesions. (**h**) Brightfield image of submucosa paired with wholemount shown in **b**. Arrows indicate lesions. Scale bar, 1 mm. Image representative of 8 wholemounts. (**i-k**) Projected confocal z stacks of stroma underlying lesions (arrowed) stained for **i**, capillary endothelial marker CD31 (green), lymphatic endothelial vessel marker LYVE-1 (magenta) and KRT14 (white); scale

bar, 200 μm. (**j,k)** Immune infiltrate in stromal wholemount stained for myeloid marker CD11b (green) and KRT14 (magenta) (**j**) and lymphoid marker CD3 (green) and KRT14 (magenta) (**k**). Scale bar, 100 μm. Each image is representative of at least 3 tumours. See **Supplementary Table 4** for source data for **d** and **e**.

Figure 3: Transcription and origin of dysplasias

(**a**) Hierarchical clustering of normalised expression values using complete linkage of transcripts from tumours and adjacent normal appearing epithelium. Heat map indicates Z scores. Arrow indicates sample of apparently normal epithelium intermediate between normal and tumour groups. (**b**) Interaction map of proteins implicated in RNA splicing encoded by transcripts downregulated in tumours. (**c**) Quantitative PCR with reverse transcription of selected transcripts in HGD compared with adjacent control epithelium, relative to *Hprt* messenger RNA. *Krt6b, Krt17* and *Sprr2f* represent differentiation-associated transcripts, *Ccnd2* proliferation-associated and Fcer1g inflammation-associated mRNAs; *Raf1* is implicated in oncogenic signalling pathway. Values are means of n=9 independent biological replicates, normalised to control (=1). Error bars are s.e.m. *P<0.05 **P<0.01; ***P<0.001 by Mann Whitney test. (**d-g**) Origin of HGD lesions. (**d**) Protocol. Single cell labelling was induced in Ahcre^{ERT}Rosa26$^{flConfetti/wt}$ mice and animals subsequently treated with DEN and Sorafenib to induce lesions. Possible outcomes are shown. Clonal lesions, derived from a single cell would be either unlabelled or completely labelled with a single colour, while the presence of multiple coloured and/or unlabelled areas would indicate multiple cells of origin. (**e**) Oblique view of 3D rendered confocal Z stack of typical lesion, dotted white line indicates lesion edge, GFP green, YFP yellow, RFP red, and Itga6 white. Scale bar, 200 μm. Image representative of 9 lesions. (**f**) Clones

per lesion (n=9 lesions from 5 animals). Line indicates mean. (**g**) Clone area (n=13 clones, from 3 lesions in 3 animals). Line indicates mean. See **Supplementary Table 4** for source data for **c**, **f** and **g**.

Figure 4: Expression of mutant Kras^{G12D} induces SCC.

(**a**) Protocol. Ah*cre*^{ERT}Rosa26$^{wt/flYFP}$Kras$^{wt/G12D}$ transgenic mice were administered DEN prior to induction of the Kras^{G12D} mutant, followed by Sorafenib treatment for 42 or 56 days. (**b**) Haematoxylin & eosin staining of representative section of typical SCC, image typical of 26 tumours. Scale bar, 250 μm. (**c**) Close up of area of invasion in **b**. Scale bar, 50 μm, T, tumour, M, muscle. (**d**) Survival of induced Ah*cre*^{ERT}Rosa26$^{wt/flYFP}$Kras$^{wt/G12D}$ (KrasG12D) and Ah*cre*^{ERT}Rosa26$^{wt/flYFP}$Kras$^{wt/wt}$ (WT) animals (P=0.0001 by Log Rank test, n=11 per group). Arrows indicate time points of sampling for clonal analysis (see **Fig. 8**). (**e**) Typical cryosection of SCC in induced Kras^{G12D} animal treated with Sorafenib, stained for Phospho-ERK (P-ERK, red) and ITGA6 (white). Scale bar, 200 μm, 100 μm, inset. (**f**) Gene expression array analysis was performed on 12 SCCs from 4 Ahcre^{ERT}Rosa26$^{flYFP/wt}$Kras$^{flG12D/wt}$ animals, induced after DEN exposure and prior to Sorafenib treatment. Hierarchical clustering of normalised expression values using complete linkage of transcripts from SCCs. Heat map indicates Z scores. (**g,h**) Quantitative PCR with reverse transcription of selected transcripts in SCC compared with control epithelium (**g**) or HGD (**h**). Transcript levels normalised relative to *Hprt* messenger RNA. *Krt6b*, *Krt17* and *Sprr2f* are differentiation-associated, *Ccnd2* and *Ctnnb1* proliferation-associated and *Myd88*, *Fcer1g* and *Ifngr2* inflammation-associated transcripts. *Raf1*, *Pten* and *Igfbp2* are implicated in oncogenic signalling. Values are means of n≥4 independent biological replicates, normalised to control (=1). Error bars are s.e.m. *P<0.05

P<0.01; ***P<0.001 by Mann Whitney test. See **Supplementary Table 4 for source data and exact P values for **d**, **g** and **h.**

Figure 5 Sorafenib accelerates tissue turnover. (**a**) Protocol. Transgenic $R26^{M2rtTA}$/TetO-HGFP mice were treated with Sorafenib and doxycycline (dox) to induce expression of a Histone2BJ-GFP fusion protein (HGFP). After withdrawal of dox, HGFP is diluted by cell division. HGFP levels were quantified at the time points shown. (**b**) Confocal images show 'top down' views of representative unstained epithelial wholemounts at indicated times. Scale bar, 20 μm. (**c**) HGFP dilution. Box plots of HGFP fluorescence intensity in at least 300 cells per animal (n=3 animals per time point, 4 animals at 72h) following Dox withdrawal. Box indicates 25^{th} and 75^{th} percentiles, centre line is median, whiskers indicate range. (**d-f**) Lineage tracing in Sorafenib treated Ah*cre*^{ERT}Rosa26$^{-/flYFP}$ transgenic mice. (**d**) Protocol. Clonal density labelling was induced (green arrow) after 28 days of Sorafenib treatment, which continued for a further 12 days. Animals were injected with EdU (purple arrow) 1 hour before being culled. (**e**) Rendered confocal z stacks of wholemounts showing representative lateral views of clones; green is YFP and white is basement membrane marker ITGA6. Scale bar, 20 μm. Image is typical example of 233 clones. (**f**) Clone size distribution (frequency of clones containing a given number of cells) in Sorafenib-treated animals, 12 days post labelling. Points are experimental data (n=233 clones from 3 animals), lines model predictions for the best fit parameters and the blue area error margins (standard deviation), see **Supplementary Note 1 and 2.2**. (**g**) Progenitor cell behaviour inferred from clone size distributions in Sorafenib and control treated animals, showing a marked increase in the cell division and stratification rates and in the proportion of divisions leading to asymmetric fates, i.e.

generating one dividing and one non-dividing cell. See **Supplementary Table 4** for source data for **c** and **f** and **Supplementary Table 5** for fitting error margins in **g**.

Figure 6 Proliferation, migration and cell retention in HGD lesions. (**a-c**) EdU lineage tracing. (**a**) Protocol. Lesions were induced and animals injected with EdU (purple arrow) 1 or 5 days before culling. (**b,c)** 'Landscape' views of rendered confocal Z stacks of wholemounts 1 day (**b**) or 5 days (**c**) after labelling; white dashed line indicates lesion margin, EdU (red), basal marker ITGA6 (white). Scale bar, 100 μm. Images are typical of 3 tumours per time point. (**d,e)** Label retention in HGD lesions. (**d**) Protocol. Lesions were generated in $R26^{M2rtTA}$/TetO-HGFP animals, followed by dox to induce HGFP expression. After dox withdrawal, HGFP diluted for 38 days. (**e**) Rendered confocal z stacks showing 'landscape' view of wholemount. Dashed white line is lesion margin. HGFP (green) and ITGA6 (white). Scale bar, 50 μm. Image is representative of 3 lesions. (**f-i**) Measuring the cell division rate in HGD and adjacent epithelium. (**f**) Protocol. Lesions were generated in $R26^{M2rtTA}$/TetO-HGFP mice. dox was then given for 4 weeks, withdrawn and samples collected over 72 hours. (**g**) Confocal image, representative of 6 lesions, from edge of dysplasia showing HGFP fluorescence (green), basal marker ITGA6 (white) and tumour associated cytokeratin KRT6 (magenta). Scale bars, 50 μm and 20 μm, respectively. Arrows indicate the border of dysplasia (HGD) and adjacent epithelium (A). (**h**) Ratio of HGFP intensities in adjacent epithelium (A) to HGD after 72 hours (n=6 lesions). (**i**) Mean cell generations (number of completed cell divisions since 24 hours post dox withdrawal) in HGD (black; n=4 animals (24h and 48h); 6 animals at 72h) and adjacent epithelium (purple; n=3 animals per time point) (see **Methods**, **Supplementary Note 2.1**, **Supplementary Fig. 6b,c**). Error bars are of the

logarithmic HGFP fluorescence levels, due to mouse-to-mouse variation (see discussion in Supplementary Note 2.1). The dashed line represents a slope of 1/day. A least-squares linear regression yields a slope of 0.99 ± 0.01 (s.e.m.)/day in HGD and 0.97 ± 0.06 in adjacent epithelium, which estimates the cell division rate (see **Supplementary Note 2.1**). See **Supplementary Table 4** for source data for **h** and **i.**

Figure 7: Cell dynamics in HGD lesions. (**a-d**) Lineage tracing in dysplastic lesions. (**a**) Protocol. After generating dysplasias in Ah*cre*^{ERT}Rosa26$^{-/flYFP}$ mice, YFP was induced at clonal density and samples imaged 13 days later. (**b**) Rendered confocal z stacks showing typical 'landscape' view, representative of 19 lesions, containing YFP+ clones (green, magenta is EdU and white is ITGA6). Scale bar, 100 μm. (**c**) Clone size distributions 13 days after induction. Points are experimental data (n=100 clones), lines model fits and blue area indicates standard deviation. Note that sizes > 40 may be attributed to clone fusions (see **Supplementary Note 2.3**). (**d)** Model: dynamics of proliferating cells (pink) in dysplasias, adjacent epithelium is shaded purple, see **Supplementary Table 5** for error margins. (**e-g**) Cell dynamics in HGD in Ahcre^{ERT}Rosa26$^{flConfetti/wt}$ mice. (**e**) Protocol. Dysplasias were generated prior to induction of the confetti reporter at clonal density. Samples were imaged 10 days or 21 days later. (**f**) Rendered confocal z stacks showing 'landscape' view of a representative example of 21 lesions containing one or more confetti clones (yellow is YFP, red RFP, magenta is DAPI). Scale bar, 100 μm. (**g**) Clone size distribution 10 days after induction. Points are experimental data (100 clones from 3 animals), line model fit and blue area indicates standard deviation (see **Supplementary Note 2.3**). (**h**) Mean Ki67+ cells as a percentage of total nucleated cells in HGD and adjacent epithelium (A) (**p<0.0072 by t-test, n = 5 tumours, from 4 mice). See **Supplementary Table 4** for source data for **c**, **g** and **h.**

Figure 8: Cell dynamics in Ras-driven SCCs.

(**a**) Protocol. Ah*cre*^{ERT}Rosa26$^{wt/flYFP}$Kras$^{wt/G12D}$ transgenic mice were administered DEN prior to simultaneous induction of the Kras^{G12D} mutant and YFP, followed by Sorafenib treatment for 42 or 56 days. (**b-d**) Examples of clones. Reconstructed 3D rendered confocal z stacks of representative clones in vibratome sections of SCCs stained for YFP (green) and ITGA6 (white). Scale bar, 100 μm. Images typical of 147 clones. (**e**) Clones per tumour (n=31 tumours, from 16 animals). Line indicates mean. (**f**) Clone sizes at 42 and 56 days after induction. (**g, h**) Clone size distributions 42 days after induction. Points are experimental data, lines model predictions and blue area indicates standard deviation. Data are binned in intervals of 10 cells per clone (**g**) and 100 cells per clone (**h**), respectively. (**g**) Clones < 150 cells (n=65 clones) overlying predictions of dysplasia model (**Fig. 7d**). (**h**) Clones > 150 cells (n=33 clones), with theoretical prediction (exponential function, see **Supplementary Note 2.4**). Clone size is rescaled (size relative to mean clone size). (**i**) Proliferating cell fate in oesophageal squamous cell carcinoma. Δ indicates cell fate bias towards producing proliferating progeny, low in smaller SCC clones (blue), higher in larger SCC clones (green). (**j**) Mean percentage Ki67+ cells/total nucleated cells in SCC and adjacent epithelium (A), (*p=0.022 by t-test, n=4 tumours). See **Supplementary Table 4** for source data for **f-h** and **j.**

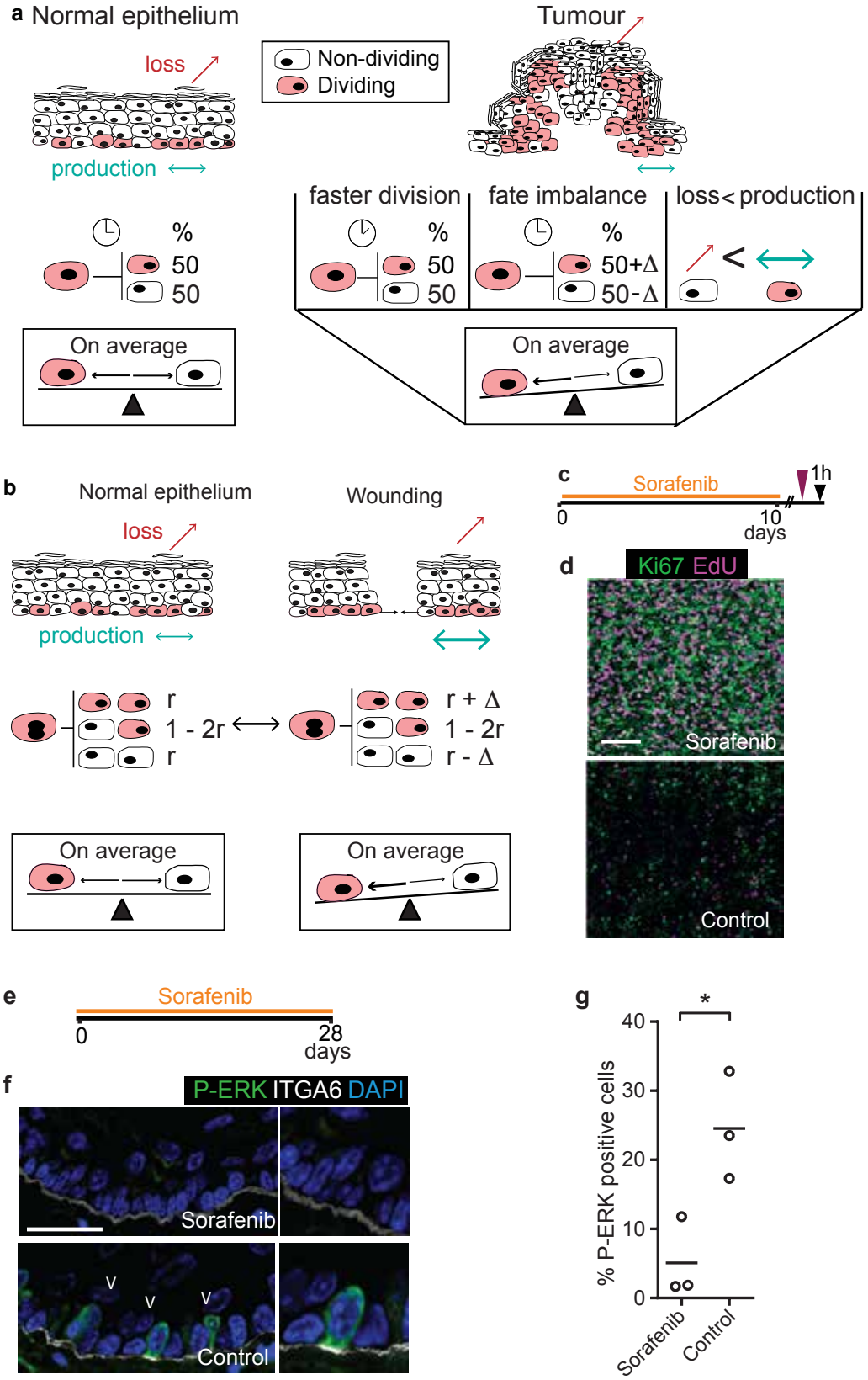
a Normal epithelium
loss
production
Non-dividing
Dividing
Tumour
%
50
50
On average
faster division
%
50
50
fate imbalance
%
50+Δ
50-Δ
loss< production
On average
b
Normal epithelium
loss
production
Wounding
r
1 - 2r
r
r + Δ
1 - 2r
r - Δ
On average
On average
c
Sorafenib
1h
0
10
days
d
Ki67 EdU
Sorafenib
Control
e
Sorafenib
0
28
days
f
P-ERK ITGA6 DAPI
Sorafenib
Control
g
*
% P-ERK positive cells
40
30
20
10
0
Sorafenib
Control

Figure-1

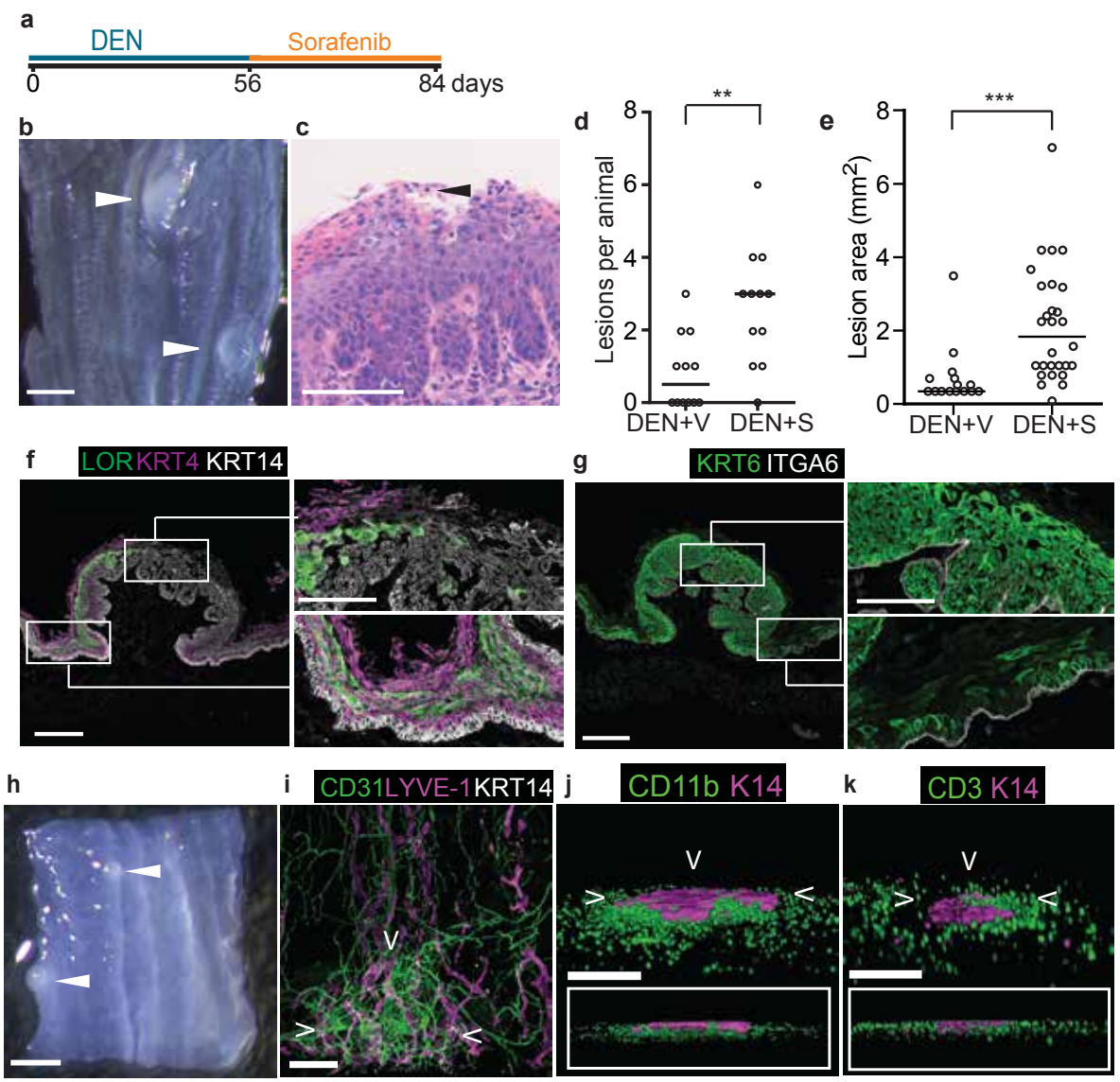
a
DEN
Sorafenib
0
56
84 days
b
c
d
Lesions per animal
**
DEN+V
DEN+S
e
Lesion area (mm2)
***
DEN+V
DEN+S
f
LOR KRT4 KRT14
g
KRT6 ITGA6
h
i
CD31 LYVE-1 KRT14
V
j
CD11b K14
V
k
CD3 K14
V

Figure-2

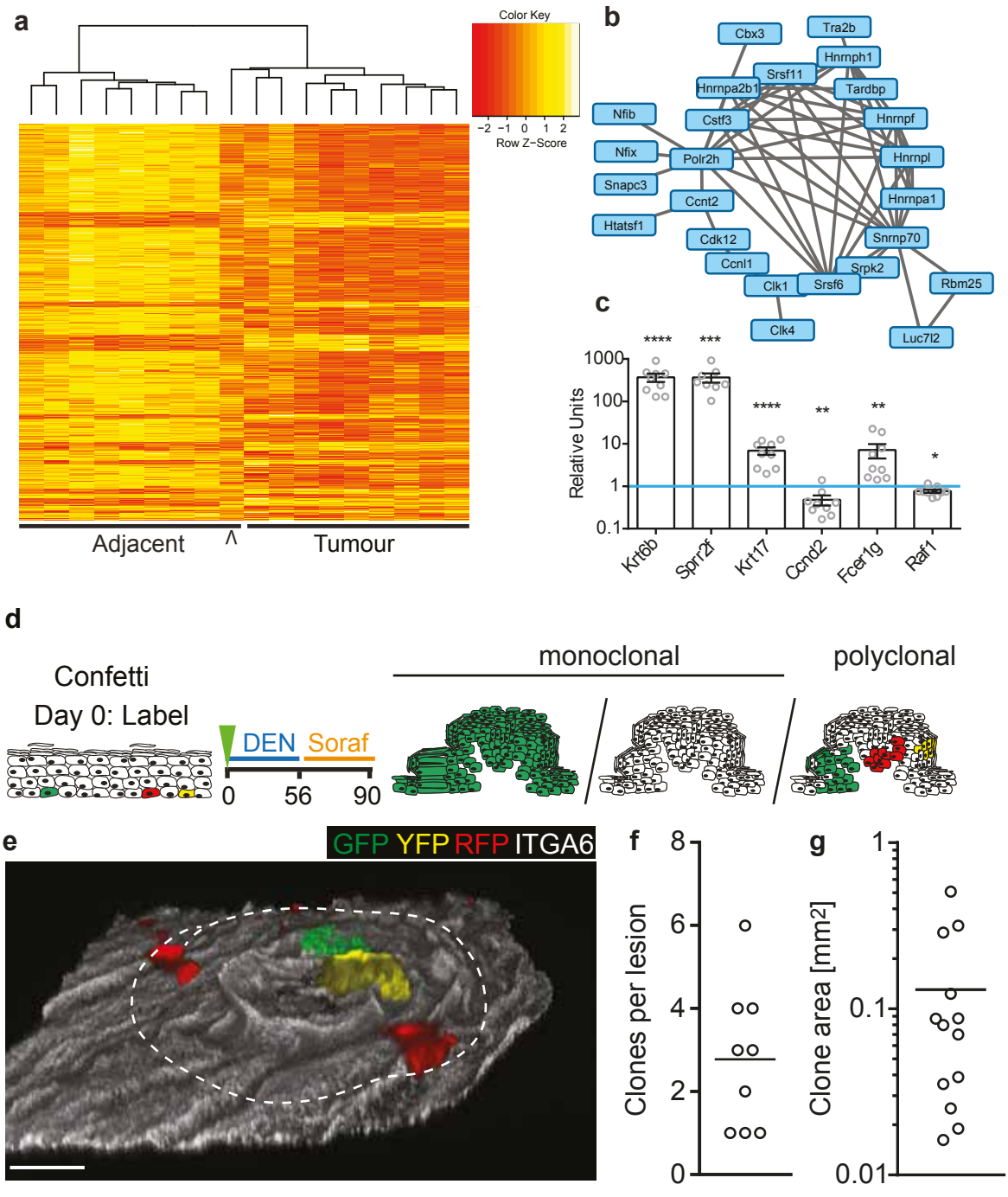
a
Color Key
−2 −1 0 1 2
Row Z−Score
Adjacent
Tumour
b
Cbx3
Tra2b
Hnrnph1
Srsf11
Hnrnpa2b1
Tardbp
Nfib
Cstf3
Hnrnpf
Nfix
Polr2h
Hnrnpl
Snapc3
Ccnt2
Hnrnpa1
Htatsf1
Cdk12
Snrnp70
Ccnl1
Srpk2
Clk1
Srsf6
Rbm25
Clk4
Luc7l2
c
Relative Units
1000
100
10
1
0.1
****
***
****
**
**
*
Krt6b
Sprr2f
Krt17
Ccnd2
Fcer1g
Raf1
d
Confetti
Day 0: Label
DEN
Soraf
0
56
90
monoclonal
polyclonal
e
GFP YFP RFP ITGA6
f
Clones per lesion
8
6
4
2
0
g
Clone area [mm²]
1
0.1
0.01

Figure-3

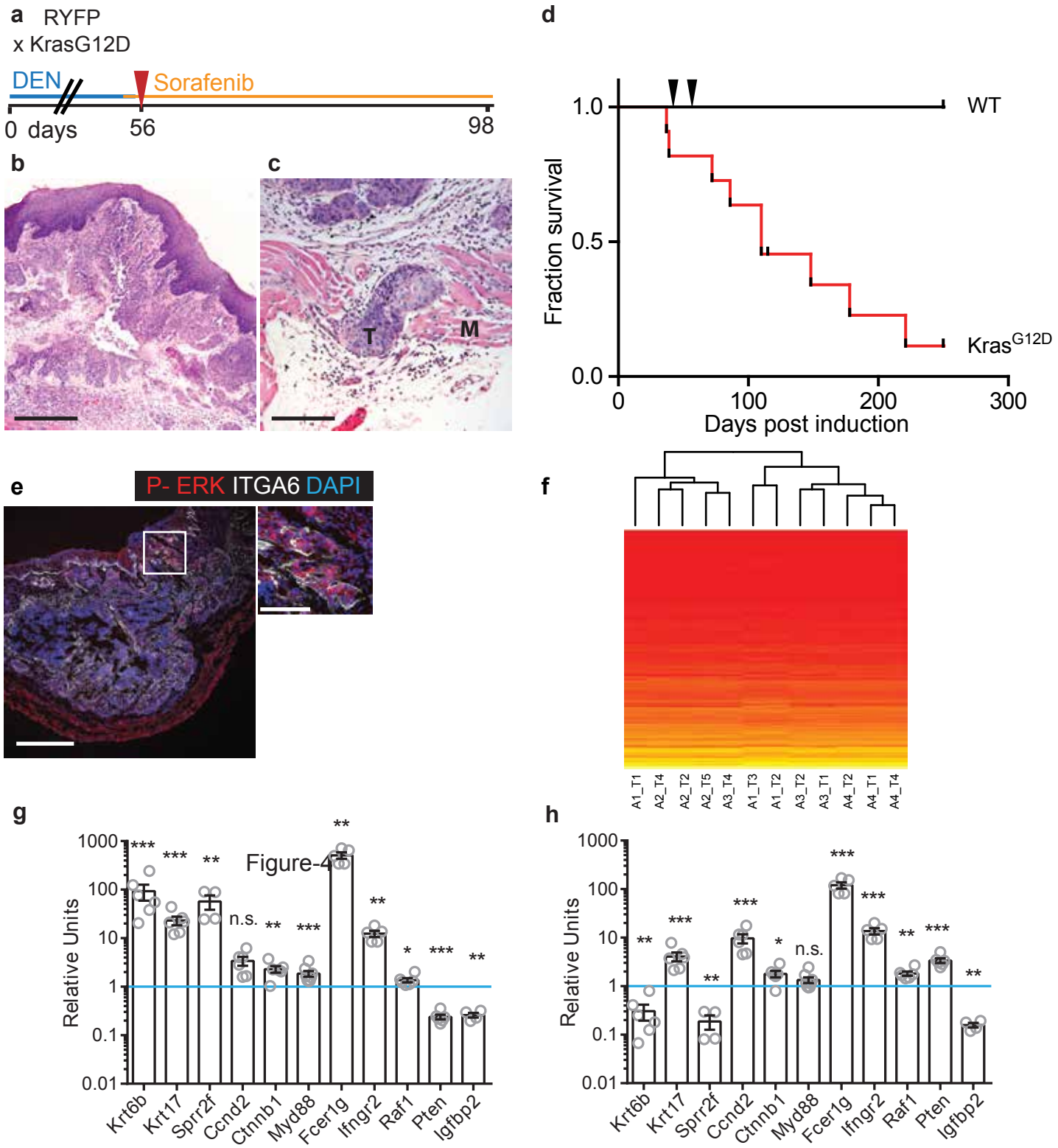
a
RYFP
x KrasG12D
DEN
Sorafenib
0 days
56
98
b
c
T
M
d
1.0
0.5
0.0
Fraction survival
WT
KrasG12D
0
100
200
300
Days post induction
e
P- ERK ITGA6 DAPI
f
A1_T1
A2_T4
A2_T2
A2_T5
A3_T4
A1_T3
A1_T2
A3_T2
A3_T1
A4_T2
A4_T1
A4_T4
g
Figure-4
Relative Units
1000
100
10
1
0.1
0.01
n.s.
Krt6b
Krt17
Sprr2f
Ccnd2
Ctnnb1
Myd88
Fcer1g
Ifngr2
Raf1
Pten
Igfbp2
h
Relative Units
n.s.

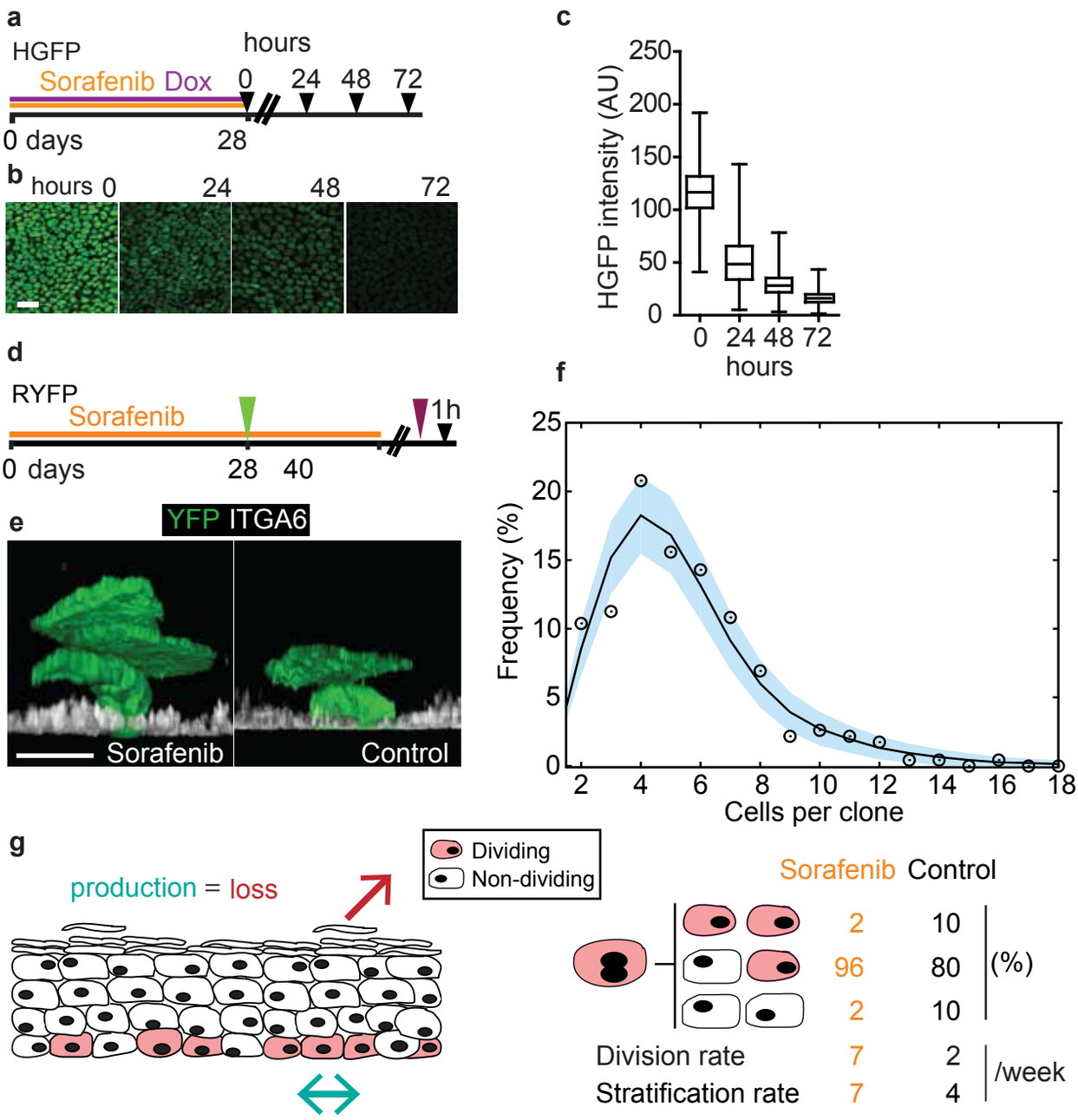
a
HGFP
hours
Sorafenib Dox
0
24
48
72
0 days
28
b
hours 0
24
48
72
c
HGFP intensity (AU)
250
200
150
100
50
0
0 24 48 72
hours
d
RYFP
Sorafenib
1h
0 days
28 40
e
YFP ITGA6
Sorafenib
Control
f
Frequency (%)
25
20
15
10
5
0
2 4 6 8 10 12 14 16 18
Cells per clone
g
production = loss
Dividing
Non-dividing
Sorafenib Control
2 10
96 80
2 10
(%)
Division rate 7 2
Stratification rate 7 4
/week

Figure-5

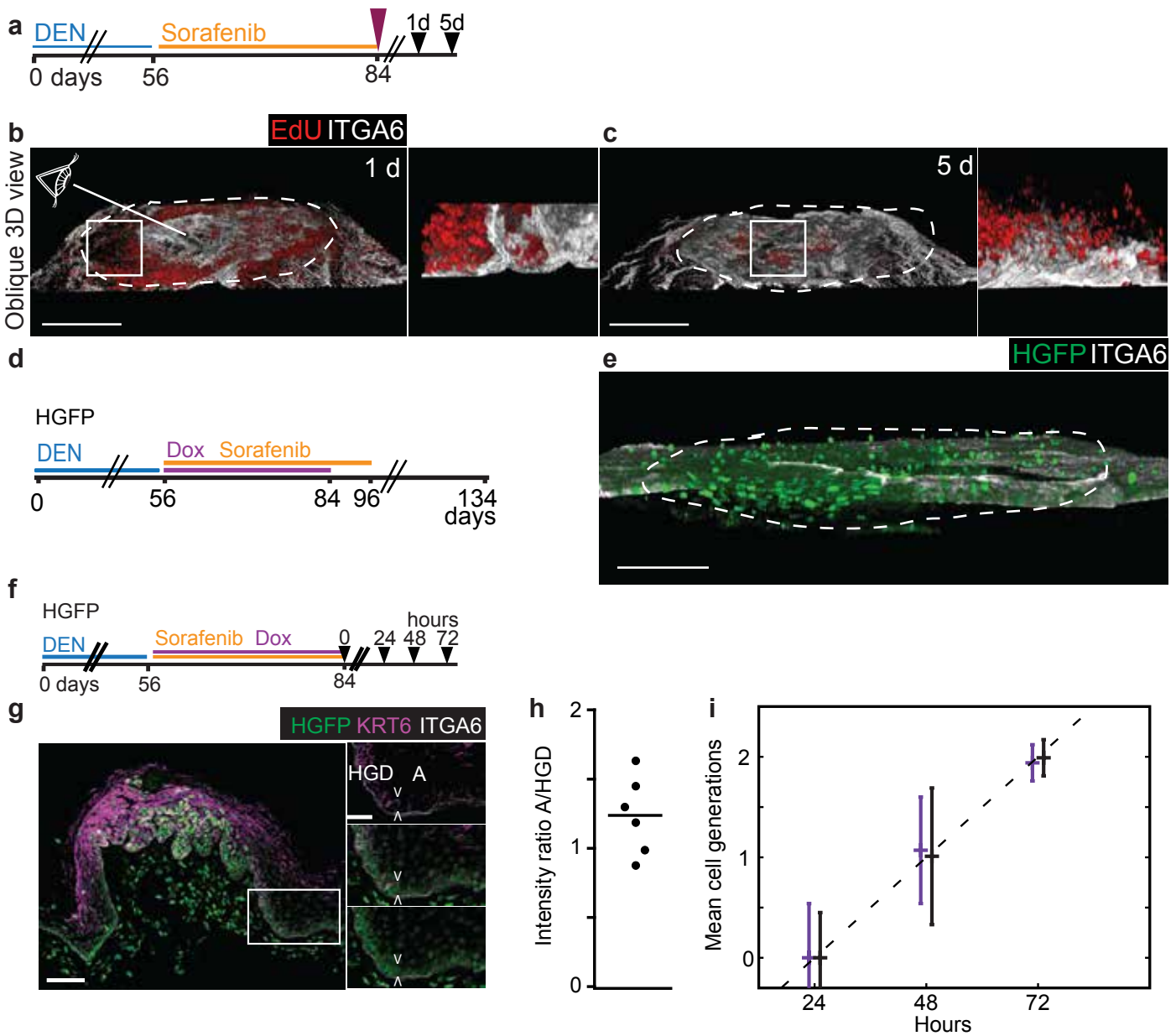
a
DEN
Sorafenib
1d 5d
0 days
56
84
b
EdU ITGA6
1 d
Oblique 3D view
c
5 d
d
HGFP
DEN
Dox Sorafenib
0
56
84 96
134
days
e
HGFP ITGA6
f
HGFP
DEN
Sorafenib Dox
hours
0 24 48 72
0 days
56
84
g
HGFP KRT6 ITGA6
HGD A
h
Intensity ratio A/HGD
2
1
0
i
Mean cell generations
2
1
0
24
48
72
Hours

Figure-6

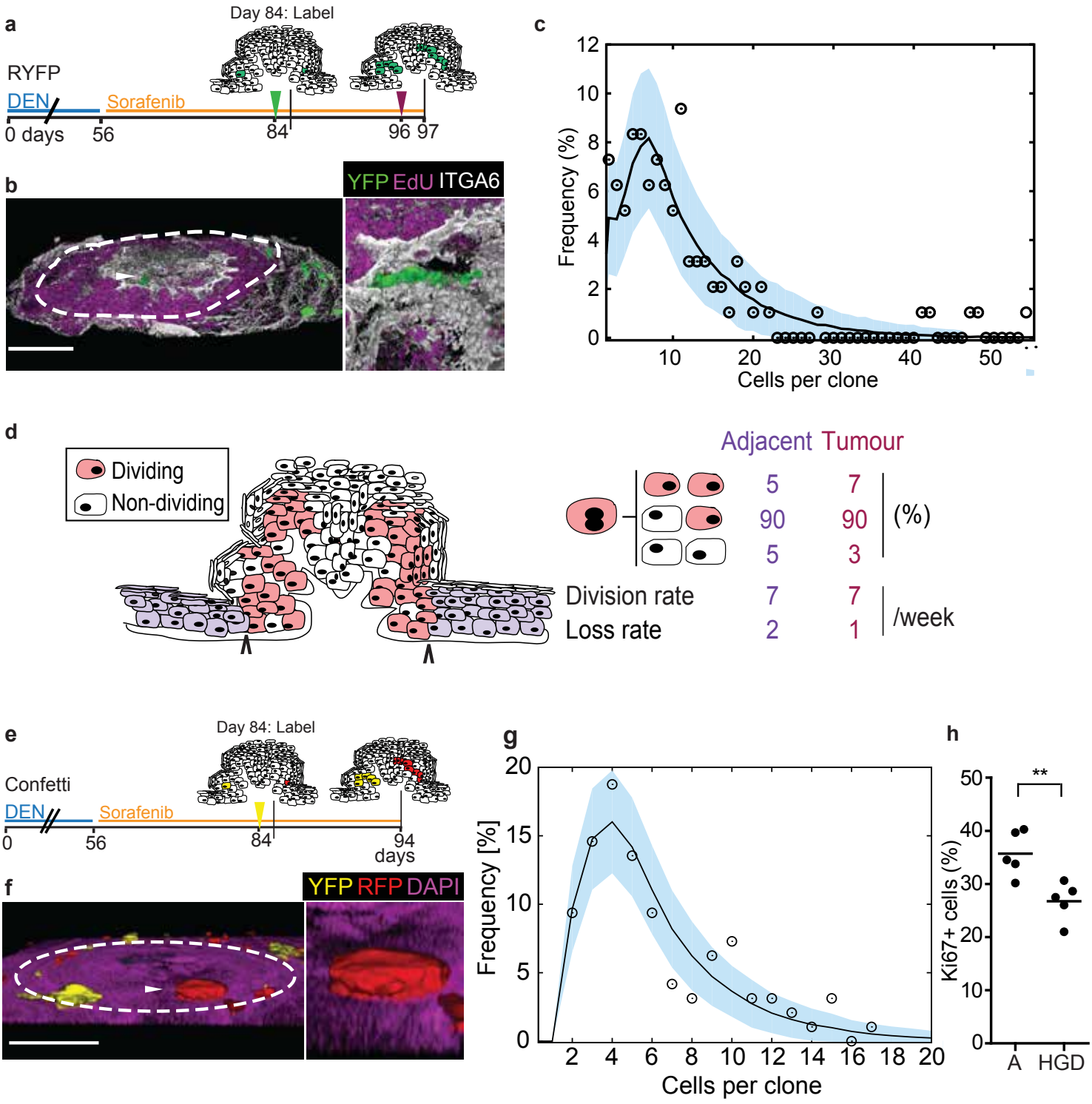
a
Day 84: Label
RYFP
DEN
Sorafenib
0 days
56
84
96 97
b
YFP EdU ITGA6
c
Frequency (%)
Cells per clone
d
Dividing
Non-dividing
Adjacent Tumour
5 7
90 90 (%)
5 3
Division rate 7 7
Loss rate 2 1 /week
e
Day 84: Label
Confetti
DEN
Sorafenib
0
56
84
94
days
f
YFP RFP DAPI
g
Frequency [%]
Cells per clone
h
Ki67+ cells (%)
**
A
HGD

Figure-7

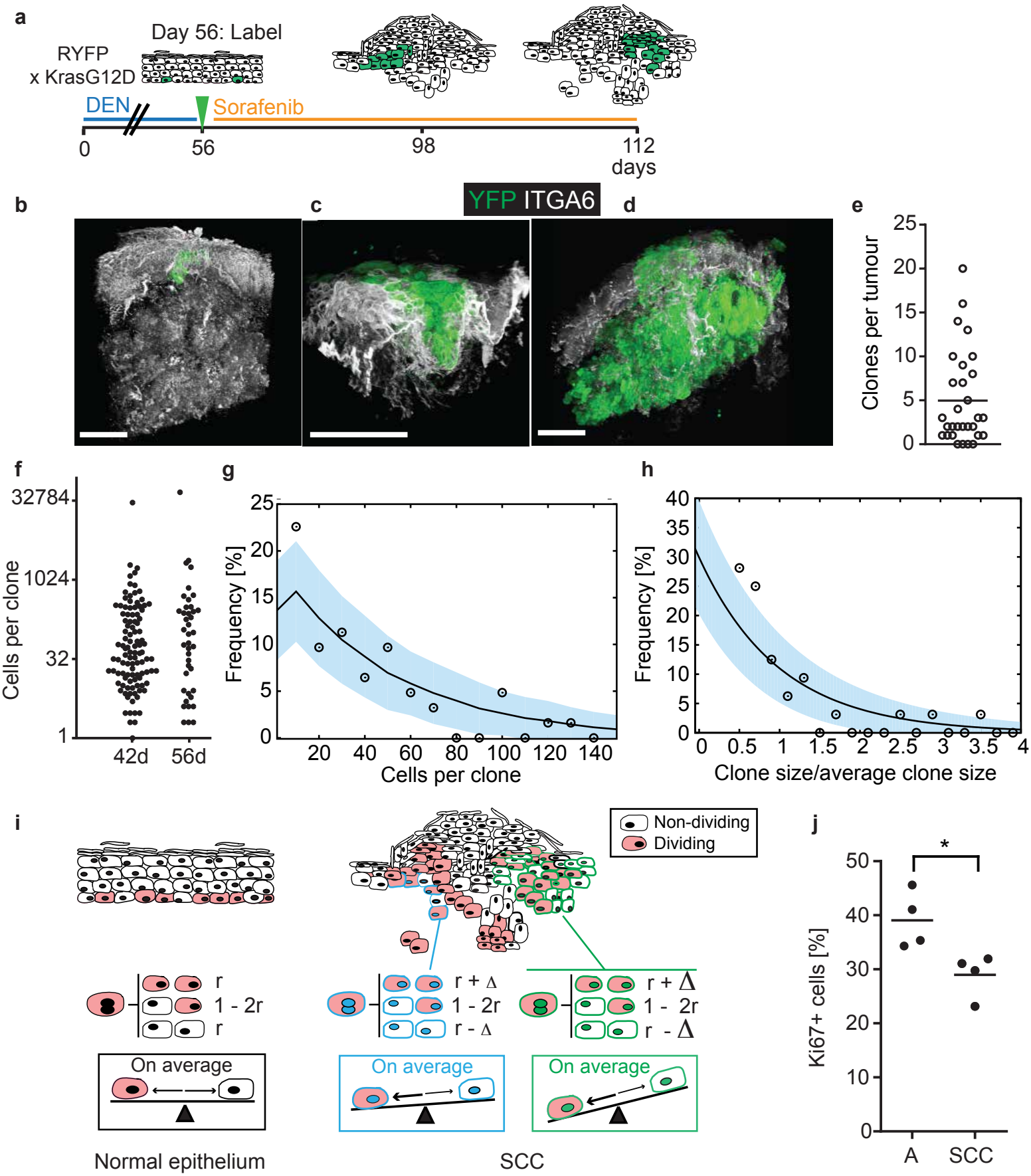
a
Day 56: Label
RYFP
x KrasG12D
DEN
Sorafenib
0
56
98
112
days
b
c
YFP ITGA6
d
e
Clones per tumour
f
Cells per clone
42d
56d
g
Frequency [%]
Cells per clone
h
Frequency [%]
Clone size/average clone size
i
Non-dividing
Dividing
r
1 - 2r
r
r + Δ
1 - 2r
r - Δ
r + Δ
1 - 2r
r - Δ
On average
On average
On average
Normal epithelium
SCC
j
Ki67+ cells [%]
*
A
SCC

Figure-8

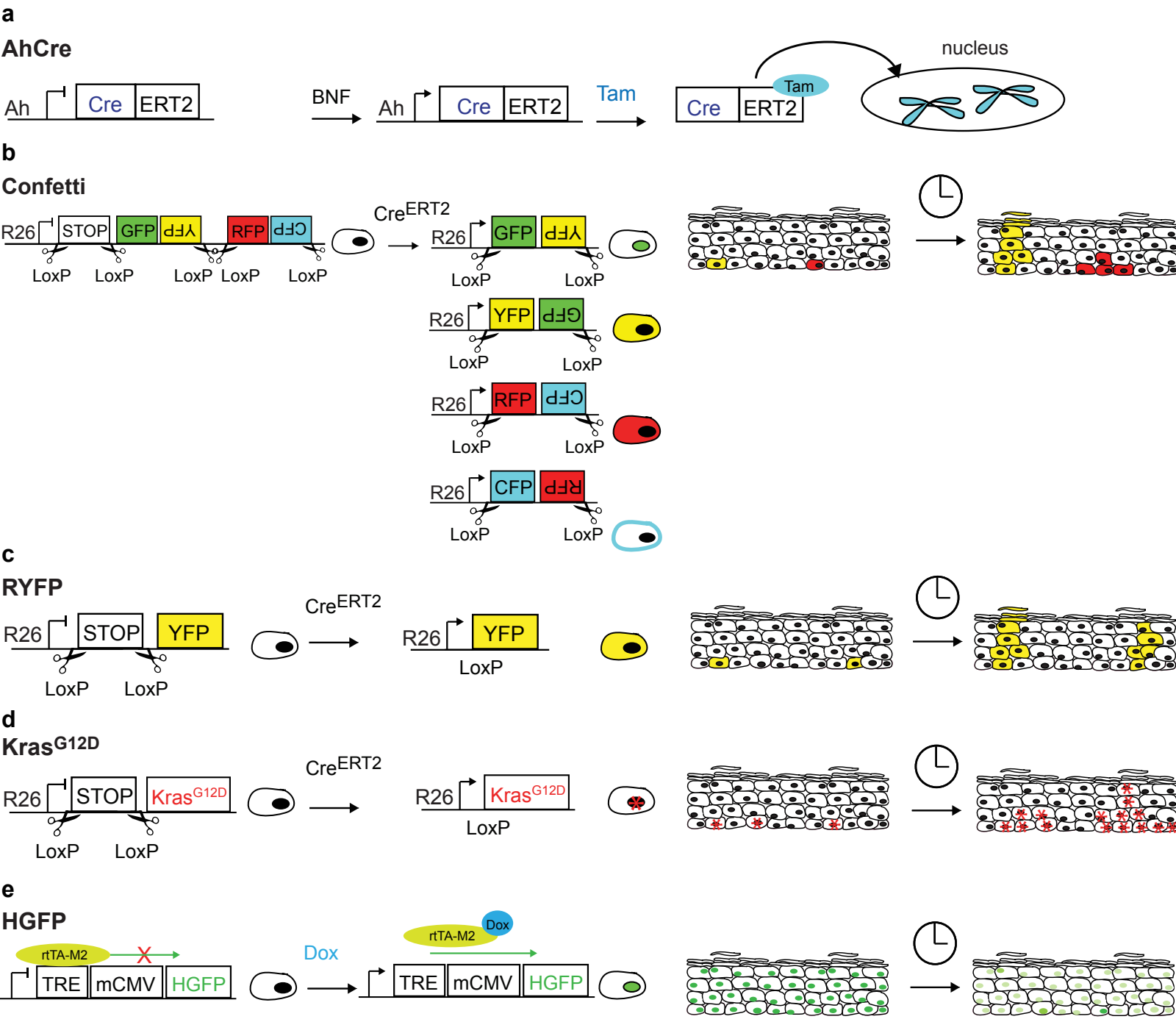

Supplementary Figure-1

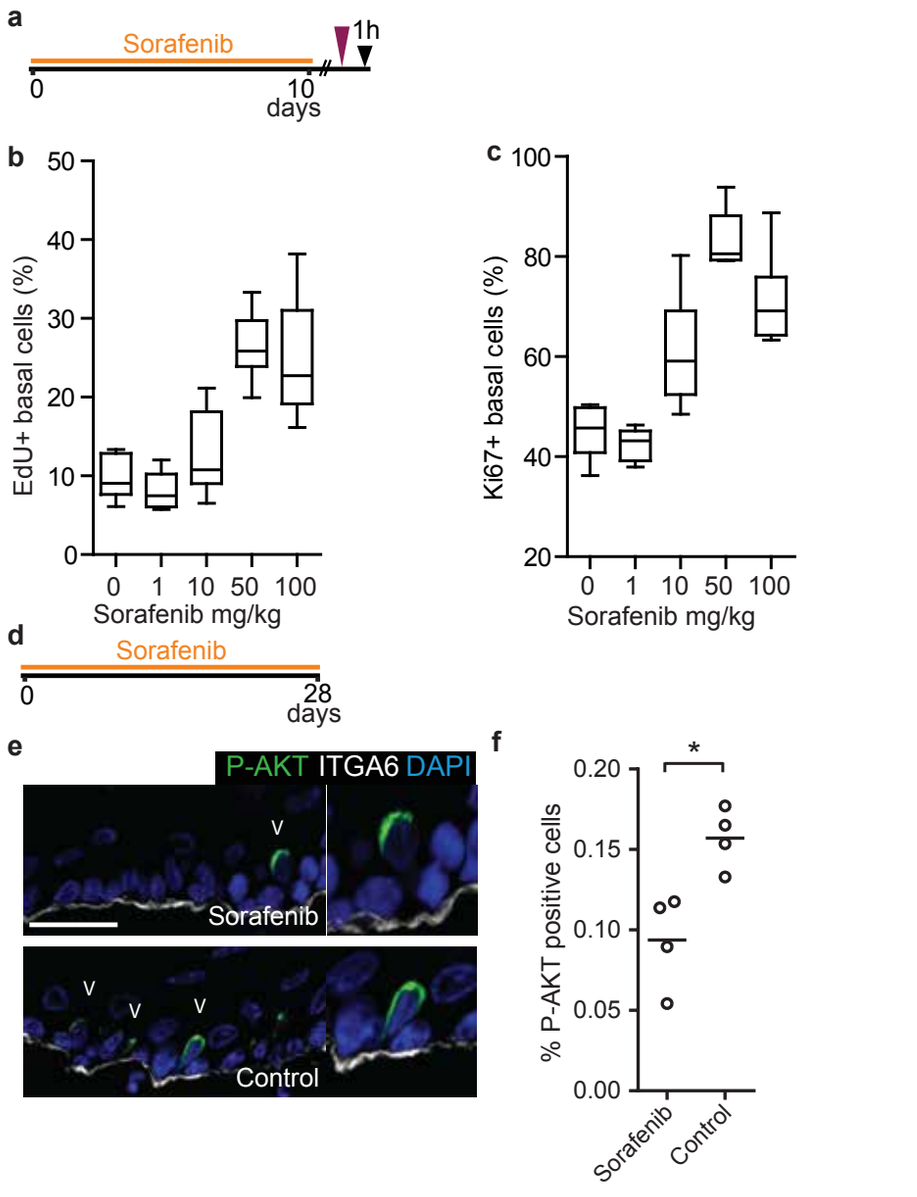

h

	% Caspase 3+	Cells counted
Sorafenib	0.001	1594
HGD	0.081	4266
SCC	0.34	55270

Supplementary Figure-2

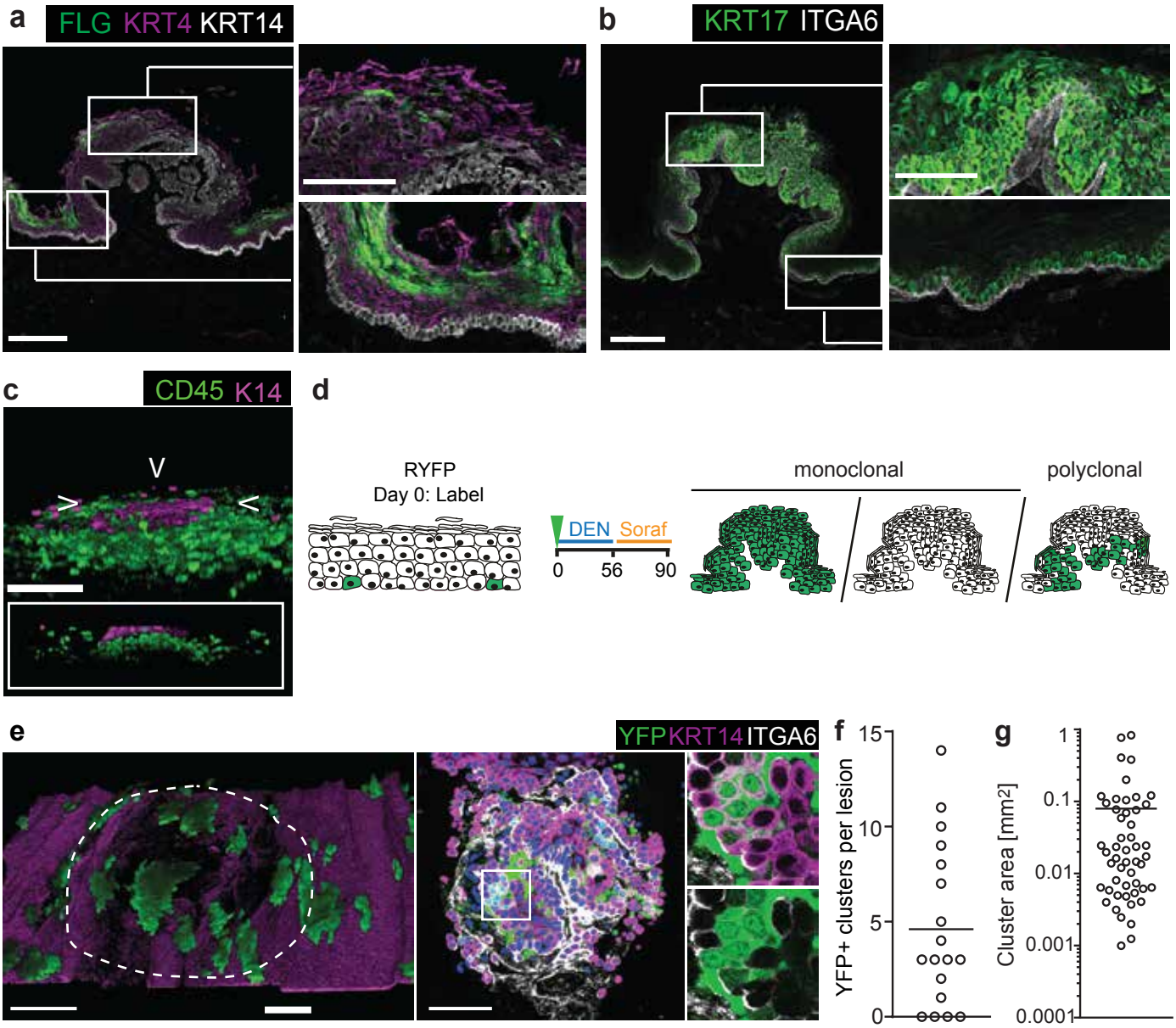

Supplementary Figure-3

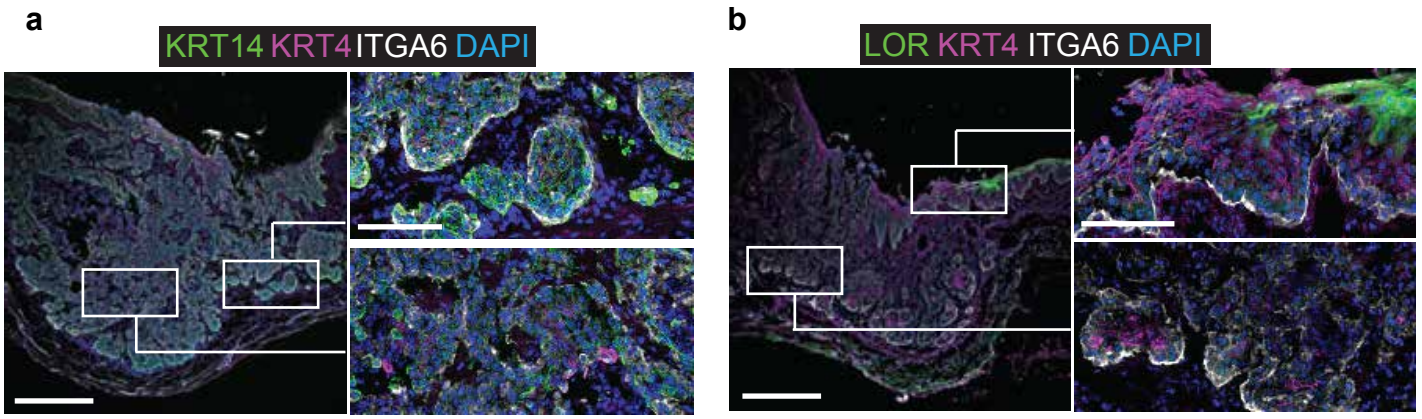

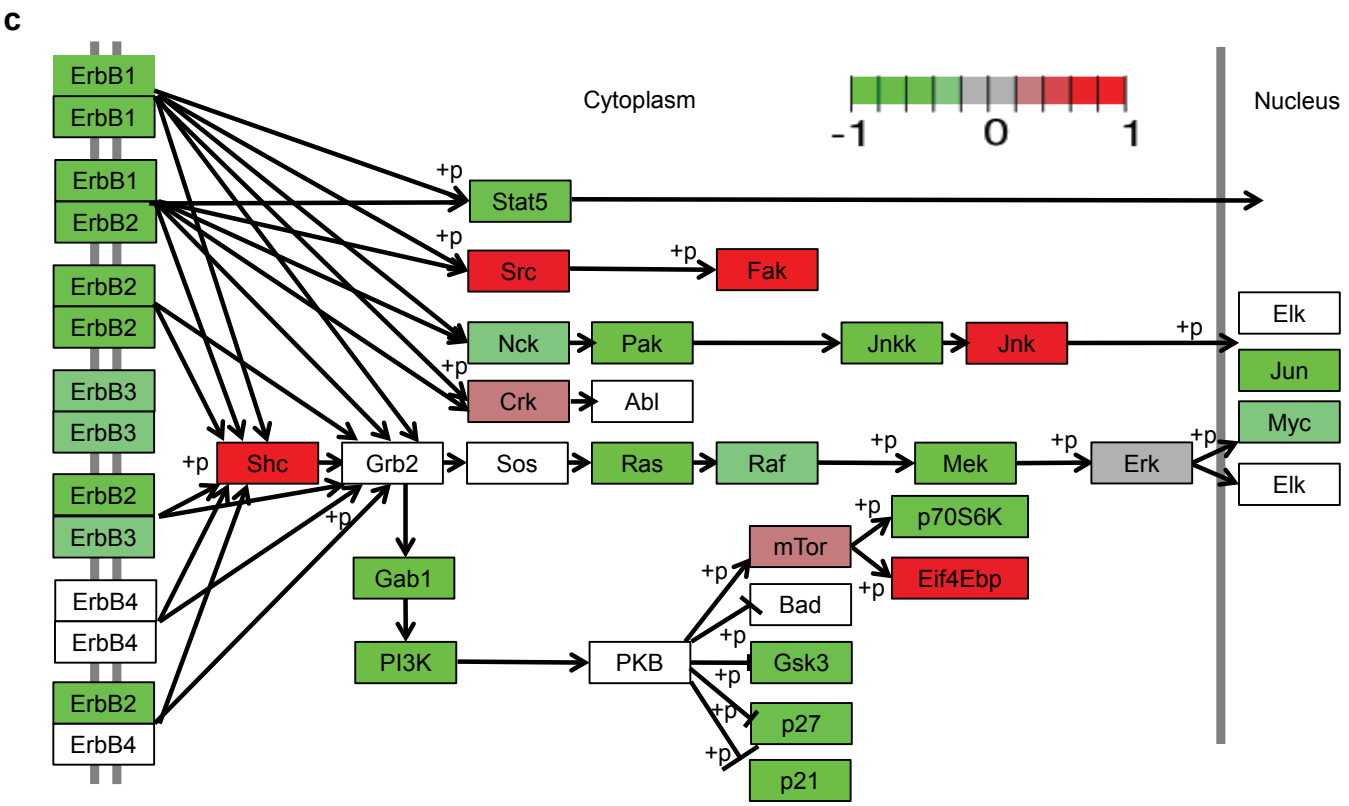

Supplementary Figure-4

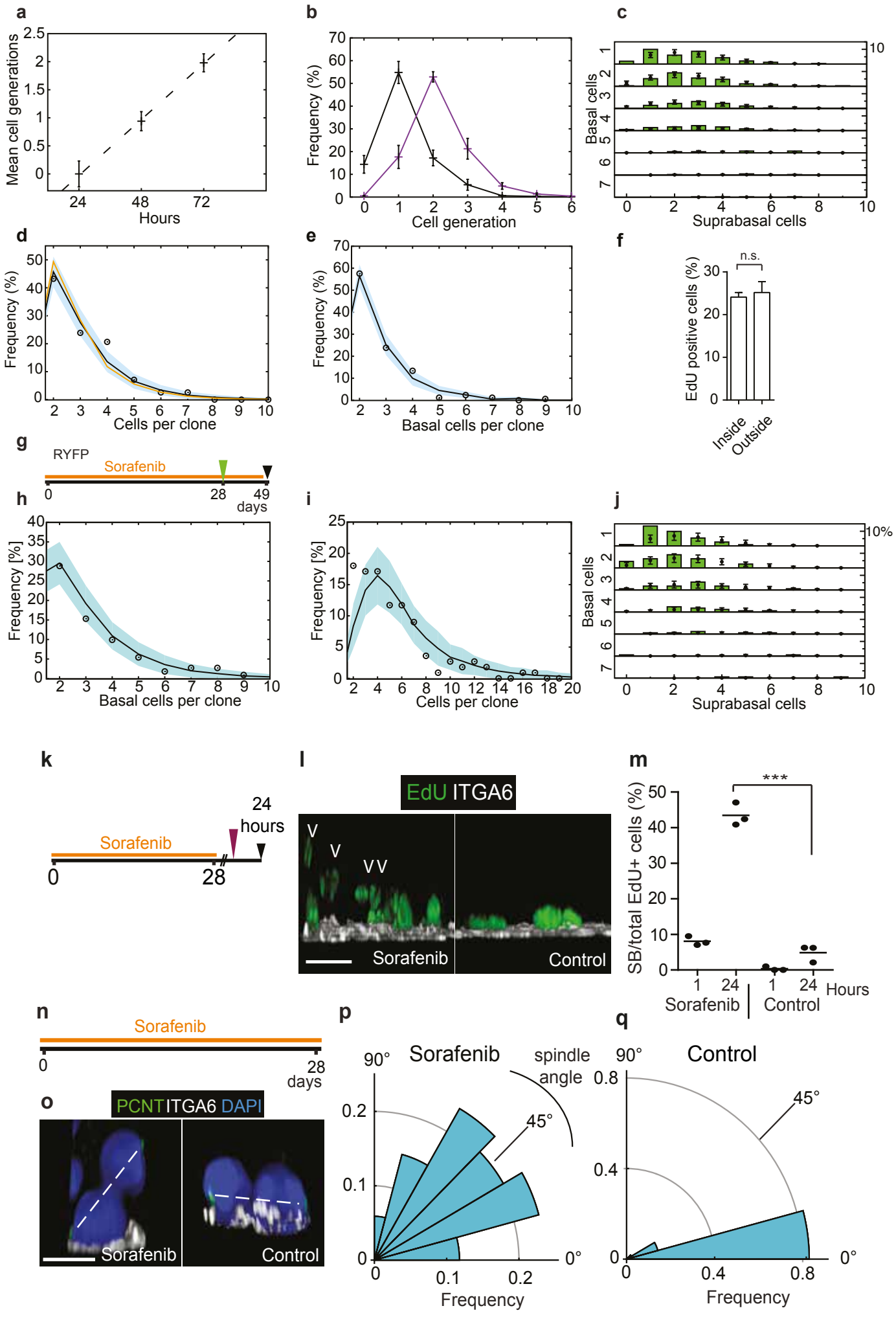

Supplementary Figure-5

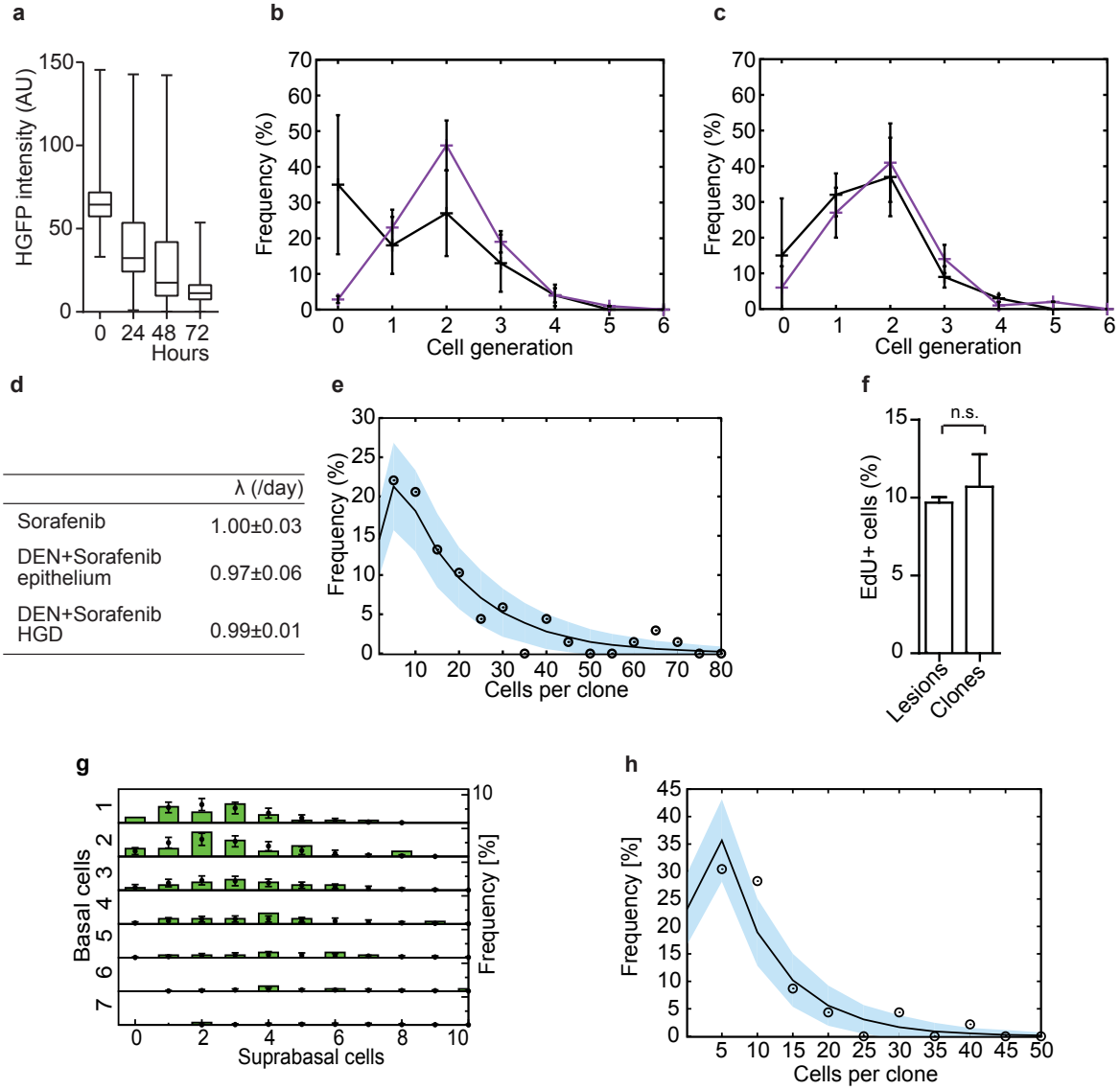

Supplementary Figure-6

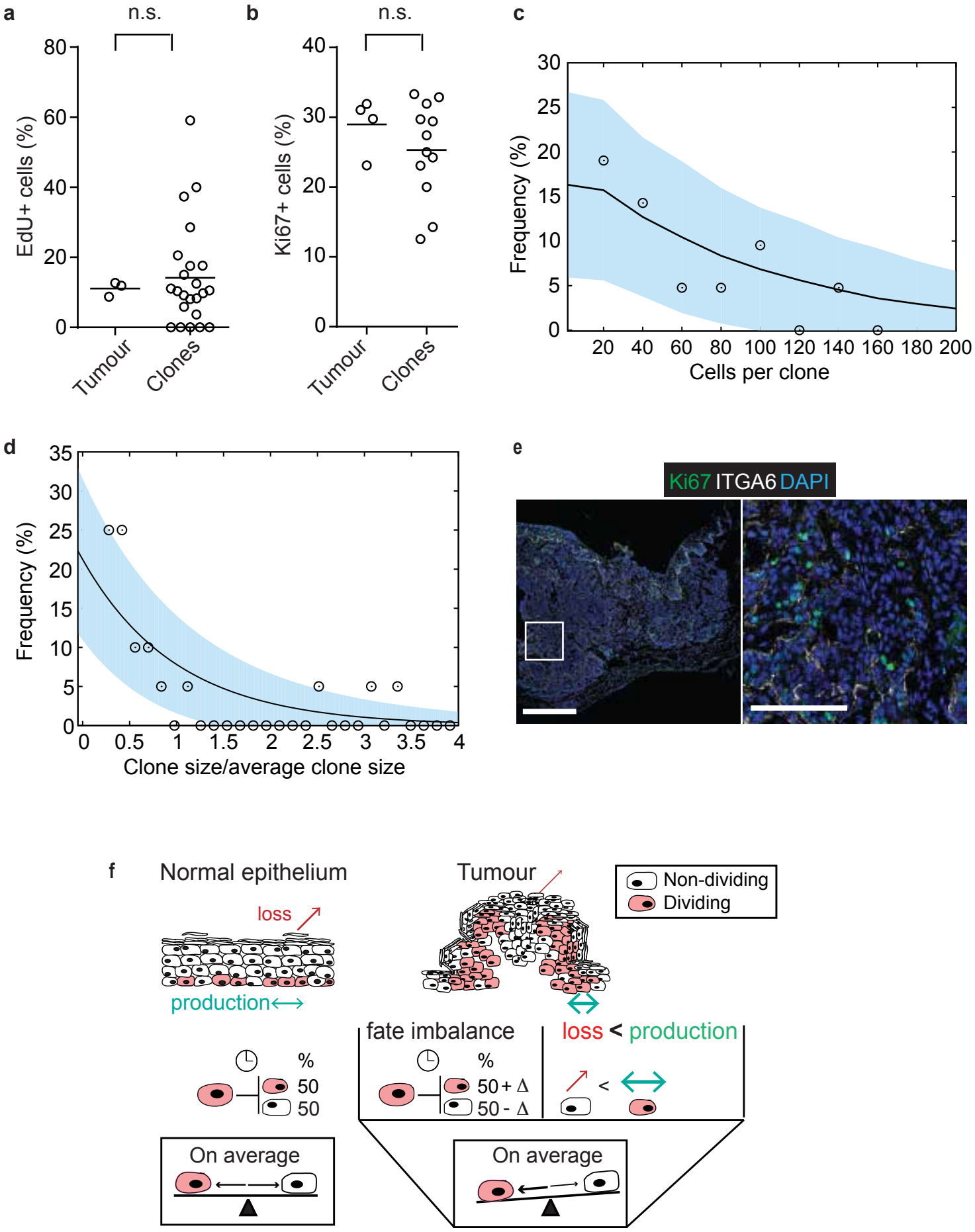

Supplementary Figure-7

Supplementary Note

In this supplementary note we outline the mathematical analysis of the data and the modelling scheme for cell fate dynamics in oesophageal epithelium treated with diethylnitrosamine (DEN) and Sorafenib. The models are challenged on data from cell lineage tracing experiments. In those experiments, clones are scored by their cell numbers (*clone size*) and from the statistical ensemble of clones, we determine the frequency distribution of clone sizes, the *clone size distribution (CSD)*. These data serve as the basis to test the validity of the models and to determine model parameters through fitting.

First, the established model for homeostatic cell fate dynamics in oesophagus (*1*) is introduced and challenged on clonal data from Sorafenib-treated tissue. For modelling the cell fate dynamics in high-grade squamous dysplasia (HGD) and invasive tumours, we suggest a simple adjustment of this model to account for cell fate imbalance and test whether this is consistent with cell lineage data.

1 Modelling and Fitting procedure

Basic model: From clonal analysis of oesophagus (*1*) it is known that progenitor cell fate evolves according to the paradigm of *stochastic cell fate* (*2, 3*). In this model, oesophageal progenitors P divide stochastically with rate λ and either daughter cell may exit cell cycle and

commit to differentiation, termed a D-cell, according to the rules

$$P \xrightarrow{\lambda} \begin{cases} P+P & \text{Prob. } r & \text{duplication} \\ P+D & \text{Prob. } 1-2r & \text{asymmetric cell division} \\ D+D & \text{Prob. } r & \text{symmetric differentiation .} \end{cases} \quad (1)$$

The probabilities of gain and loss of progenitor cells, given by the fate outcomes $P \rightarrow P + P$ and $P \rightarrow D + D$ must be equal to achieve homeostasis. Following division, D-cells may migrate to the suprabasal layers (*stratification*, with rate γ), then denoted as D^*-cells.

$$D \xrightarrow{\gamma} D^* \qquad \text{(stratification) .} \quad (2)$$

Finally, cells progress toward terminal differentiation, and eventually lose their nuclei (with rate σ), after which they are considered lost

$$D^* \xrightarrow{\sigma} \emptyset \qquad \text{(loss of nucleus) .} \quad (3)$$

This model has been shown to describe clonal dynamics in normal oesophagus (*1*). Here we test if these cell fate rules also hold for tissue challenged by the treatment of Sorafenib. For that purpose, the quantitative predictions for clonal evolution are compared with the experimentally obtained clone size distributions (CSDs). We employ *stochastic simulations*, using a Gillespie algorithm (*4*), to compute the time evolution of clones. In these simulations, the stochastic rules **1 - 3** are applied starting with a single progenitor cell, and the statistical distribution of clone sizes is determined. The model outcome is then compared to the data, and the Bayesian certainty of the model parameters is computed to assess the goodness of the model, as described in the following. In section 2.3 we show that cell fate dynamics in HGD can be recovered by a slight adjustment of this model, by allowing cell fate imbalance between duplication and exit of cell cycle. In that scenario, however, D-cells only partially differentiate.

The presented model is a paradigmatic example for the neutral competition of progenitor cells within an equipotent progenitor cell population. Note that other implementations of this

paradigm, for example one allowing reversible priming of progenitor cells for differentiation or proliferation, may lead to similar predictions on clonal statistics. Yet, such details of the dynamics could not be resolved by the available cell lineage data, and thus we focus here on the simpler question whether the paradigm of a single equipotent progenitor population is sustaining the tissue renewal and tumour growth. The model used here is one representative of this more broadly defined class of cell fate dynamics.

Fitting procedure: For fitting the model to the data, we follow a Bayesian approach, similar to the one used to infer cell fate rules in normal oesophageal epithelium (*1*). The certainty of a set of parameter values $\theta = (\lambda, r, \gamma, \sigma)$ [1], in view of the data $\mathcal{D}$, can be quantified by the *Bayesian certainty* (also called *Bayesian posterior probability*)

$$P(\theta|\mathcal{D}) = \mathcal{N}\, P(\mathcal{D}|\theta)\, P(\theta) \tag{4}$$

where $P(\mathcal{D}|\theta) =: L(\theta)$ is the likelihood of θ, i.e. the probability that the model with parameter values θ reproduces the data, and the *prior* $P(\theta)$ is the *a priori* certainty of the model parameters, without taking into account $\mathcal{D}$. The factor $\mathcal{N} = \sum_\theta P(\mathcal{D}|\theta)P(\theta)$ is a normalisation for the probability. The prior $P(\theta)$ is an estimate of the parameter certainty due to information from other sources, e.g. previous measurements. We choose as a prior the distribution with maximal entropy, matching the given information. Without further information this is a uniform distribution; if a mean and variance is known, and the variance is much smaller than the mean[2], we choose a normal distribution as prior.

In our case, we have additional information on cell kinetics by measurements of *Histone-GFP (HGFP)* dilution (see section 2.1) which restricts the possible range for the cell division rate. In these measurements the cell division rate is determined with mean $\bar{\lambda}$ and standard error

[1] For the later introduced model of clonal dynamics in dysplasia (section 2.3), parameters differ: $\theta = (\lambda, r, \mu, \delta)$.

[2] Strictly speaking, a gamma distribution would be the maximum entropy prior. If the standard deviation is small compared to the mean, however, this can be approximated by a normal distribution.

σ_λ by linear regression. The maximum entropy prior for given mean and standard error is a normal distribution

$$P(\theta) = \frac{1}{\sqrt{2\pi\sigma_\lambda^2}} \exp\left[-\frac{(\lambda-\bar{\lambda})^2}{2\sigma_\lambda^2}\right] \quad . \tag{5}$$

The model with parameters θ predicts the probabilities $p_{b,s}(\theta)$ to observe clones with b basal and s suprabasal cells. The data is given in the form of the *detailed clone size distribution (detailed CSD)* $\mathcal{D} = \{f_{b,s}\}_{b,s}$, where $f_{b,s}$ is the frequency of measured clone sizes with b basal and s suprabasal cells. Under the model assumptions, the probability to observe a clone with (b, s) cells exactly $f_{b,s}$ times follows a multinomial distribution

$$L(\theta) = P(\mathcal{D}|\theta) = \frac{[\sum_{b,s} f_{b,s}]!}{\prod_{b,s} f_{b,s}!} \times \prod_{b,s} p_{b,s}(\theta)^{f_{b,s}} \quad , \tag{6}$$

as shown in the supplementary note of Ref. (*1*). When only the total cell number per clone is available from the data, $\mathcal{D} = \{f_n\}$, Eq. **6** is evaluated with a single index n instead of b, s. Note that only clones with more than one cell are counted to eliminate the possibility of counting induced D-cells (cf. discussion in Ref. (*1*)). With the results of simulation and Eq. **6**, the likelihood of parameters θ is computed and the Bayesian certainty determined with the prior $P(\theta)$ taken from the HGFP measurements. When data from different time points is available, the full likelihood is obtained by multiplying the individual likelihoods of each time point.

To find the set of best fit parameter values $\theta^* = (\theta_1, \theta_2, ...)$, the parameter space is 'scanned' on a close-meshed grid in intervals $\Delta\theta_i$ from minimal values $\theta_i^{\min}$ to maximum values $\theta_i^{\max}$, and the Bayesian certainty $P(\theta|\mathcal{D})$ is determined for each θ (see Ref. (*5*) for details). For each set of parameters, $n = 150000$ clones are simulated and the Bayesian certainty is determined according to Eq. **6**, and the prior, Eq. **5**. The benchmarks of the parameter space scan are given in Table 1. The parameter values θ^* with the maximum Bayesian certainty, $P^* := P(\theta^*|\mathcal{D})$, are chosen as best fit parameter values.

In order to determine error margins for parameters, we compute the root-mean-squared

deviation of parameters from θ^* when distributed according to the Bayesian posterior probability distribution that has been determined as described above. For that purpose, n=10000 parameter value points θ^α ($\alpha = 1, ..., n$) are generated randomly, following the Bayesian posterior probability distribution. The error of each parameter θ_i is then computed as $\delta\theta_i = \sqrt{n^{-1}\sum_{\alpha=1}^{n}(\theta_i^\alpha - \theta_i^*)^2}$.

Error margins of data points in clone size distributions: Since the abundance of clones of a given clone size may be very small in the experimental data, it is subject to substantial statistical noise. In order to obtain the range of deviations from the expected clone frequencies, we simulate by our model the data fluctuations due to small clone sample numbers. In that process, we run the stochastic simulations n = 1000 times repeatedly, taking the best fit parameters θ^* and simulate the same total clone number as counted in the lineage tracing experiments. Each sample simulation j gives a prediction for the clone frequencies $f_{b,s}^j$ of finding b basal and s suprabasal cells, and we take the standard deviation of the set $\{f_{b,s}^j\}_j$ as the error margin. These error margins are shown in the following plots of the CSDs as error bars (detailed CSDs) or blue shaded areas (total/basal cell CSDs), which mark the expected range of the deviations between data and model prediction.

We have also checked the mouse-to-mouse variations in the clone counts and found that they are comparable to the error originating from small sample size error.

2 Data analysis and model fitting results

In this section we analyse the HGFP fluorescence data to obtain estimates for the cell division rate, and we fit cell fate models to clonal data from oesophageal epithelium that has been disturbed by various measures (administration of Sorafenib and DEN). The best fit parameter values and parameter error margins will be determined according to the procedure described in

the last section (rates in units of $1/w$ = per week, or $1/d$ = per day).

2.1 Cell division rate from analysis of the HGFP dilution data

In the HGFP dilution experiments, HGFP production is arrested at time point $t = 0$ when administration of Doxycycline is stopped. Samples are harvested at 24, 48 and 72 hours afterwards. During cell division, HGFP is partitioned equally between daughter cells so that a cell that has divided i times contains on average a concentration of 2^{-i} times the initial concentration of HGFP. The number of cell cycles i a given cell has traversed since a given time point t_0 (the *cell generation*) can thus be obtained from the HGFP fluorescence intensity f, as $i = \log_2(f_0/f)$, where f_0 is the fluorescence at time t_0. Here we will use $t_0 = 24$ hours as the reference time, as argued below. By measuring the fluorescence levels for an ensemble of basal cells we determine the frequency distribution of cell generations and the mean cell generation.

Our aim is to determine the average cell division rate of proliferating cells. However, the ensemble of HGFP-labelled cells may also contain non-dividing cells, which cannot be distinguished from progenitor cells. Without further analysis, scoring the fluorescence of all cells can therefore distort the average, which is meant to be over progenitor cells only. Therefore we need to correct for non-dividing cells, as will be outlined in the following.

Denoting by n_i the mean number of progenitor cells and m_i the mean number of non-dividing cells in generation i, respectively, the time evolution of the cell populations in each generation reads

$$\begin{aligned} \partial_t n_0 &= -\lambda\, n_0 & \partial_t m_0 &= -\gamma\, m_0 \\ \partial_t n_i &= \lambda\,(n_{i-1} - n_i) & \partial_t m_i &= \lambda\, n_{i-1} - \gamma\, m_i \end{aligned} \tag{7}$$

where λ is the cell division rate, and γ the stratification rate of non-dividing cells. It is assumed that progenitor cells are not immediately lost, and that cell fate imbalance does not play a

significant role over the short time periods (3 days) considered in the HGFP dilution assay. By measuring HGFP fluorescence levels of each cell, we can only determine the total fraction of cells in a given generation i, $z_i = n_i + m_i$, not of individual cell types. The mean cell generation of all cells, $\bar{i} := Z^{-1} \sum_i i\, z_i$, is related to the mean cell generation of progenitor cells $\bar{i}_P := N^{-1} \sum_i i\, n_i$, and of non-dividing cells $\bar{i}_D := M^{-1} \sum_i i\, m_i$ ($Z := \sum_i z_i$, $N := \sum_i n_i$, $M := \sum_i m_i$) through

$$\begin{aligned} \bar{i} &= \frac{1}{Z} \sum_i i\,(n_i + m_i) = \frac{N}{Z}\frac{1}{N} \sum_i i\, n_i + \frac{M}{Z}\frac{1}{M} \sum_i i\, m_i \\ &= \rho\, \bar{i}_P + (1-\rho)\, \bar{i}_D \ , \end{aligned} \tag{8}$$

where $\rho := N/Z$ is the fraction of progenitor cells. The means $\bar{i}_{P,D}$ have the time evolution

$$\begin{aligned} \partial_t \bar{i}_P &= \frac{1}{N} \sum_i i\, \partial_t n_i = \frac{\lambda}{N} \left(\sum_{i=1}^{\infty} i\, n_{i-1} - \sum_{i=0}^{\infty} i\, n_i \right) \\ \partial_t \bar{i}_D &= \frac{1}{M} \sum_i i\, \partial_t m = \frac{1}{M} \left(\lambda \sum_{i=1}^{\infty} i\, n_{i-1} - \gamma \sum_{i=0}^{\infty} i\, m_i \right) \ . \end{aligned} \tag{9}$$

With the substitution $i \to i+1$ we have

$$\sum_{i=1} i\, n_{i-1} = \sum_{i=0} (i+1) n_i = N(1 + \bar{i}_P) \ , \tag{10}$$

so that

$$\begin{aligned} \partial_t \bar{i}_P &= \lambda \\ \partial_t \bar{i}_D &= \frac{\lambda N}{M} (1 + \bar{i}_P) - \gamma\, \bar{i}_D \ . \end{aligned} \tag{11}$$

With $\bar{i}_{P,D}(t = t_0) = 0$, and since in the stationary state $N/M = \gamma/\lambda$, we get the solution of these ordinary differential equations

$$\begin{aligned} \bar{i}_P(t) &= \lambda\, t \\ \bar{i}_D(t) &= \lambda\, t - \lambda/\gamma + 1 + e^{-\gamma t} (\lambda/\gamma - 1) \ . \end{aligned} \tag{12}$$

Differentiating for t and substitution of this result in Eq. **8** gives

$$\partial_t \bar{i} = \lambda - (1-\rho)\,\gamma\, e^{-\gamma t}\,\left(\frac{\lambda}{\gamma} - 1\right) \approx \lambda \qquad \left(\text{for } t \gg \frac{1}{\gamma}\right) \tag{13}$$

Hence, the slope of the time course of the mean cell generation of *all* cells is a good approximation for the cell division rate λ of progenitor cells for large times $t \gg \gamma$, or if $\lambda \approx \gamma$.

Since the result depends only on the time derivative of the mean cell generation – which does not depend on f_0 – we can define the reference fluorescence level f_0 as the fluorescence at 24 hours, thus counting cell generations from day 1 after Dox withdrawal. Thereby uncertainties in the time scale of Dox withdrawal are avoided.

The mean cell generation, defined as $\bar{i}(t) = \langle \log_2(f_0/f(t)) \rangle$, is shown as a function of time in Supplementary Fig. 5a for Sorafenib-only treated tissue and in Fig. 6i for tissue treated with DEN and Sorafenib, both inside and outside of the dysplastic region. Since for each animal, measurements can only be obtained at a single time point, but the definition of the cell generation involves two time points, no measurements of the cell generations in individual animals is available. Despite this, the mean value of i can be obtained from averaging the logarithmic fluorescence at individual time points over different animals, as $\bar{i} = \langle \log_2(f_0) \rangle - \langle \log_2(f) \rangle$. However, the exact s.e.m. of i cannot be obtained from the data alone, since we have no information about the correlation of f_0 and $f(t)$ for individual animals. Instead we chose to give the s.e.m of $\langle \log_2(f) \rangle$ at individual time points in Supplementary Fig. 5a and Fig. 6i, which give an upper estimate of the s.e.m of i, but implicitly include variations of initial fluorescence levels. The true s.e.m. of the cell generations can be indirectly inferred from the residuals of the model fit (see below and Supplementary Fig. 6d).

We see in Supplementary Fig. 5a and Fig. 6i that the data points follow a straight line with constant slope for each case. This suggests, according to Eq. **13**, that we are in the regime where the slope of $i(t)$ approximates the cell division rate well. With this approximation, a

linear regression yields in all three cases a cell division rate very close to once per day. The results of the fitting and error margins (standard deviation of the fit's χ^2-distribution) are shown in Supplementary Fig. 6d, as well as the corresponding residuals which estimate the s.e.m. of the individual data points. In the following we will use this information for constructing a Bayesian prior for fitting the clonal data. As a maximum entropy prior with given mean and variance, we use a Gaussian function $P(\lambda) = (2\pi\sigma_\lambda^2)^{-1/2}\exp(-(\lambda-\bar{\lambda})^2/(2\sigma_\lambda))$ where $\bar{\lambda}$ is the best fit value of the regression and σ_λ its standard error (see Supplementary Fig. 6d).

The distributions of cell generation times are shown in Supplementary Figs. 5b,6b,c for Sorafenib-only treatment, DEN+Sorafenib treatment inside HGD, and DEN+Sorafenib treatment in tissue adjacent to HGD, respectively. Remarkably, for Sorafenib-only treatment, the generation distributions keep their shape and are merely shifted by one cell cycle between subsequent days which indicates that cell cycle times are highly uniform with a length of 24 hours. This would be expected if cell divisions were limited by the circadian clock and is consistent with the strong diurnal regulation of proliferation in the oesophagus (*6*).

2.2 Clonal analysis in Sorafenib-treated tissue

In the first experiment, animals were pre-treated with Sorafenib for 28 days before clones were induced, and tissue was harvested 12 days later. In order to infer cell fate dynamics in tissue treated with Sorafenib, we fit the parameters of the model according to the procedure outlined in section 1. The benchmarks of the fitting procedure (scanning the parameter space for determining the Bayesian certainty distribution) are given in Table 1. The resulting best fit parameter values and root-mean-square errors are given by

$$\lambda = 7.0 \pm 0.2/w \quad r = 0.02 \pm 0.01 \quad \gamma = 6.8 \pm 0.9/w \quad \sigma = 2.6 \pm 0.2/w \quad , \tag{14}$$

The error margins denote root-mean-square deviations from the best fit values as described in section 1.

(a)

parameter	$\theta_i^{\min}$	$\theta_i^{\max}$	$\Delta\theta_i$
$\lambda\,[w^{-1}]$	6.4	7.6	0.2
r	0	0.075	0.005
$\gamma\,[w^{-1}]$	4.0	10.4	0.2
$\sigma\,[w^{-1}]$	1.6	4.0	0.2

(b)

parameter	$\theta_i^{\min}$	$\theta_i^{\max}$	$\Delta\theta_i$
$\lambda\,[w^{-1}]$	5.6	8.0	0.4
r	0	0.075	0.005
$\gamma\,[w^{-1}]$	4.0	10.4	0.2
$\sigma\,[w^{-1}]$	1.6	4.0	0.2

(c)

parameter	$\theta_i^{\min}$	$\theta_i^{\max}$	$\Delta\theta_i$
$\lambda\,[w^{-1}]$	6.90	7.10	0.05
r	0.10	0.085	0.005
$\mu\,[w^{-1}]$	0.3	2.2	0.1
δ	0	1.0	0.1

Table 1: Benchmarks of scanning the parameter space for obtaining Bayesian certainties for **(a)** tissue from animals treated with Sorafenib only, **(b)** tissue from animals treated with DEN and Sorafenib, adjacent to dysplasia, **(c)** dysplastic tissue from animals treated with DEN and Sorafenib. The respective models were simulated and Bayesian certainties determined, for a close-meshed set of parameters: the parameter space was scanned in a grid with scanning interval between parameter values, $\Delta\theta_i$, minimum, $\theta_i^{\min}$, and maximum parameter values, $\theta_i^{\max}$, as given in the table. For DEN+Sorafenib treatment in dysplasia, clones with size larger than 40 are neglected for determining Bayesian certainties. These outliers are consistent with the expected range of clone fusions, as argued in the text.

The detailed CSD, showing distinct basal and suprabasal cell numbers, which was used for the fitting, is displayed for Sorafenib-treated mice in Supplementary Fig. 5c. The corresponding total CSD, comprising basal and suprabasal cell numbers in a clone, are shown in Fig. 5f. The model fits show excellent agreement with the experimental data.

To verify the model and the best fit parameters we tested its prediction on clonal data of the same experiment but clones harvested 21 days after clonal induction. The results for the joint CSD are shown in Supplementary Fig. 5j, for the basal CSD in Supplementary Fig. 5h, and for the total CSD in Supplementary Fig. 5i, giving a good agreement between model and data, thereby confirming the results of our fit.

Note that our model does not account for the apparent low variation of cell cycle times, as inferred from the HGFP data analysis in the previous section. To test whether this changes the model predictions for clone size distributions, we simulated a version of the model in which the timing between consecutive cell divisions is fixed. In this simulation, cells divide at discrete time points in intervals $1/\lambda$. To assure that the proportion of progenitor cells ρ is the same as for stochastic divisions, D-cells stratify between two cell divisions with probability $p_\gamma = \rho = \gamma/(\lambda+\gamma)$. This can be seen by checking the stationary state condition for the mean number of D-cells:

$$m_{t+1} = (m_t + n_t) - p_\gamma\,(m_t + n_t) = m_t \;\; \Rightarrow p_\gamma = \frac{n_t}{m_t + n_t} = \frac{\gamma}{\lambda + \gamma} \;\; . \tag{15}$$

where the latter identity is derived from the stationary state condition of the stochastic model $\lambda\, n_t = \gamma\, m_t$. For the best-fit parameters for Sorafenib treatment, **14**, the predicted basal CSD (counting basal cells per clone only) is shown and compared with the results from the stochastic model in Supplementary Fig. 5d. No significant difference between the two implementations can be seen within the error margins of the data.

In a control experiment, mice were given the vehicle without Sorafenib, and clones were

harvested after 12 days. If the vehicle does not affect cell fate dynamics itself, the model with parameter values from normal oesophageal epithelium (*1*) should reproduce the clonal data of this control experiment. Assuming cell cycle times of normal tissue, only three cell cycles have on average been completed after 12 days. While our stochastic model does not capture the synchronicity in differentiation of suprabasal cells at short times (after a few cell cycles), the stochastic fate of basal cells is well reproduced by the model with normal-tissue parameters, if clones with a single basal cell are excluded[3]. This is shown in Supplementary Fig. 5e, where the basal CSD from the experiment and model predictions for parameters of normal oesophageal epithelium, taken from Ref. (*1*), are compared.

Comparing the best fit parameters for tissue from Sorafenib-treated mice with normal tissue (see Supplementary Table 5), we see that the ratio of symmetric cell divisions r is significantly decreased, so that almost all cell divisions ($1 - 2\,r = 96\%$) result in asymmetric fate outcome. Furthermore, both the stratification rate and the cell division rate are significantly increased.

2.3 Clonal analysis in tissue treated with Sorafenib and DEN

For studying cell fate dynamics in HGD, mice were treated with DEN for 8 weeks, and then Sorafenib was administered for 4 weeks before clones were induced. 13 days and 22 days after induction the mice were culled and clones counted.

Clonal analysis in tissue surrounding HGD: We scored clones collected from tissue surrounding HGD, taken 13 days after induction and fitted the model parameters to the detailed CSD, according to the program of section 1. The benchmarks of scanning the parameter space to find best-fit values and error margins are shown in Table 1. The best fit parameter values and

[3]Compare detailed discussion in Ref. (*5*), where it is argued that the stochastic model describes the dynamics of basal cells well even after short times, if single basal cells are neglected.

root-mean-square errors of this fit are:

$$\lambda = 6.8 \pm 0.4/w \quad r = 0.05 \pm 0.01 \quad \gamma = 7.0 \pm 1.3/w \quad \sigma = 2.6 \pm 0.3/w \tag{16}$$

The corresponding detailed CSD is shown, together with the data, in Supplementary Fig. 6g, which shows an excellent agreement. As expected, we see that these best fit parameter values are not very different from the case of Sorafenib-only treatment; there is an overlap of the acceptable parameter regimes, except for a slightly significant difference in the symmetric division ratio r. Thus, DEN treatment does not markedly alter cell fate dynamics in non-dysplastic tissue.

Clonal analysis in HGD: Inside HGDs we expect cell fate dynamics to be non-homeostatic. In this case, we sought for the minimal adjustment of the homeostatic model that could capture the clonal dynamics, by assuming normal cell fate dynamics of the form given by rules **1**, but with a tilt towards proliferation:

$$P \xrightarrow{\lambda} \begin{cases} P+P & \text{Prob. } r(1+\delta) & \text{duplication} \\ P+D & \text{Prob. } 1-2r & \text{asymmetric cell division} \\ D+D & \text{Prob. } r(1-\delta) & \text{symmetric cell cycle exit} \end{cases}, \tag{17}$$

where δ quantifies the tilt in cell fate [4] ($\delta = 0$ corresponds to homeostasis $\delta = 1$ implies absence of symmetric cell cycle exit). Furthermore, we accommodate the observation that proliferating cells are also found in the suprabasal layers of the dysplastic epithelium and that non-dividing cells show signs of early differentiation, but terminal differentiation is suppressed. Therefore, we do not explicitly distinguish between basal and suprabasal cells in the model, and we only consider one type of non-dividing cell D, irrespective of the distance to the basement membrane and differentiation stage. Non-dividing D-cells are shed with *loss rate* μ:

$$D \xrightarrow{\mu} \emptyset \ . \tag{18}$$

[4] Note that in Supplementary Table 5, where best fit parameter values are given, the value of the absolute cell fate bias $\Delta := r\,\delta$ is given.

Note that loss of D-cells may thus occur before terminal differentiation. In order to compare this with the loss of cells in normal stratified epithelium, we need to find a corresponding quantity in latter case. We note that $\mu = 1/\tau$, where τ is the mean "life time" of a D-cell, from birth to loss. For scenarios in which basal and suprabasal cells are distinguished, the mean life time is $\tau = 1/\gamma + 1/\sigma$. Thus, in this case, the absolute loss rate is $\mu = (1/\gamma + 1/\sigma)^{-1}$ and the values for the different scenarios can be compared, as given in Supplementary Table 5.

To fit the model, we compared the distributions of total clone sizes (*total CSD*) between model and experiment, according to Eq. **4**, at both 13 and 22 days post-induction (multiplying likelihoods at both time points). The benchmarks of scanning the parameter space to find best-fit values and error margins are shown in Table 1. The resulting best fit parameter values and root-mean-square errors are given by:

$$\lambda = 7.0 \pm 0.1/w \quad r = 0.05 \pm 0.02 \quad \mu = 0.9 \pm 0.7/w \quad \delta = 0.4 \pm 0.2 \quad . \tag{19}$$

With these parameter values, the corresponding plot of the clone size distribution (model prediction and data) is shown in Fig. 7c for clonal data 13 days after induction and in Supplementary Fig. 6e for data collected 22 days after induction. Due to low numbers for fixed clone size, the clone counts at 22d after induction were binned in intervals of width 5 $\{[0, 5], [6, 10], ...\}$.

The simulation results with the best fit parameters match well both the clonal data at 13 days and at 22 days post-induction, apart from a few outliers with very large clone size. However, it cannot be excluded that clones merge, forming polyclonal clusters that cannot be distinguished, due to identical colours. We therefore repeated the experiment with mice carrying a confetti allele, which allows randomly labelling with four different colours, thereby reducing the probability that clones with the same colour merge. Fitting this clonal data gives the best fit parameters

$$\lambda = 6.95 \pm 0.05/w \quad r = 0.03 \pm 0.015 \quad \mu = 2.0 \pm 0.3/w \quad \delta = 0.7 \pm 0.3 \quad . \tag{20}$$

where the error ranges denote the standard deviation of the Bayesian posterior. In this fit a single outlier with clone size 59 cells was excluded from the data at 21 days after induction. Fig. 7g and Supplementary Fig. 6h shows the corresponding clone size distributions 10 and 21 days after clonal induction, showing good agreement between model and data. The parameters from fitting both the single colour and the confetti assay are similar with overlapping error ranges in the parameters λ, r, and δ. However, the loss rate μ is significantly higher for the confetti mouse data, which may be explained by the higher sensitivity for differentiated cells in the single colour assay.

Furthermore we check theoretically whether the outliers in the single-colour data are within the range of expected clone fusion events. Fig. 6b,c shows almost circular whole-mounts of lesions, in which proliferating cells are at the rim of HGD lesions while non-dividing cells flow radially towards the centre, relative to the growing rim. Thus we estimate that the width of a clone in angular direction of the lesion is entirely determined by the number of progenitor cells in that clone. Since there are no clones spanning the lesions across the centre, and no arc-shaped clones have been detected, we conclude that clones only merge in angular direction. 13 days after induction, we found on average 5.32 clones per HGD, with an average lesion circumference of $l = 2.23$ mm. Since the mean cell diameter is 0.01 mm, this corresponds to a clone frequency of $\phi = 0.024$ clones per peripheral cell. For the analysis we define the position of a clone as the point that is furthest clockwise at the rim. A given clone A does not touch its next neighbour clone B in anti-clockwise direction, if both clones are further apart from each other than the width s of clone A (in angular direction). Then the probability of two neighbouring clones being separated is

$$\bar{P}_t = \sum_{s=1}^{\infty} (1-\phi)^s \, P(s, \bar{s}) \tag{21}$$

where $P(s, \bar{s})$ is the probability distribution of clone widths (mean clone width $\bar{s}$), which, ac-

cording to our assumption above, corresponds to the distribution of progenitor cell numbers in a clone. According to our model, the progenitor cells perform a supercritical branching process which follows the distribution $P(s,\bar{s}) = e^{-s/\bar{s}} \times (e^{1/\bar{s}} - 1)$ (*7*). With a cell division rate of $\lambda = 7.0/w$ and a loss rate of $\mu = 0.9/w$ (best fit values) we have an equilibrium fraction of proliferative cells of $\rho = \mu/(\mu+\lambda) = 11.4\%$ in a clone. 13 days after induction, the mean size of clones is $n_{13} = 9.57$, yielding $\bar{s} = \rho\, n_{13} = 1.09$. From Eq. 21 we then get $\bar{P}_t = 0.961$, corresponding to an expected fraction of merged clones of $P_t = 1 - \bar{P}_t = 3.9\%$. We see 5 clones out of 100 counted (5%) to lie outside the error margin of the model prediction for the data taken 13 days after induction and 4 out of 68 (5.9%) after 22 days. This is is well consistent with the expected fraction of clone fusions for Poisson statistics with standard deviation $\sigma = \sqrt{5}$ and $\sigma = 2$ counts for 13 and 22 days respectively. Thus, the outliers in the data are not significantly different from what would be expected as frequency of random clone fusion events.

Remarkably, despite the expected high genetic heterogeneity due to mutagen treatment, the model can well reproduce the data with a single type of progenitor cells. The majority of cell divisions is yet asymmetric ($1 - 2\,r = 90\%$), and the tilt in cell fate is small, in terms of an excess in symmetric duplications of $2\,r\,\delta = 4\%$. A comparison of the cell fate parameters between different scenarios (normal, vehicle-treated, Sorafenib-treated, and DEN+Sorafenib-treated tissue) is shown in Supplementary Table 5.

2.4 Kras-induction and Sorafenib administration after treatment with DEN

In the final experiment, an oncogenic Kras mutant was induced together with YFP after 8 weeks of DEN administration. When clones were induced, also Sorafenib treatment started. Invasive tumours emerged, and at 42 and 56 days after induction clones were scored in those tumours.

The number of clones that could be recorded is scarce and the computational effort required

for effective model fitting is too high to perform because of the large clone sizes. Yet we can check whether the cell fate paradigm of pre-malignant lesions in oesophagus prevails. To assess this, we first checked whether some clones follow the same dynamics as clones in pre-malignant DEN-induced HGD, despite of Kras activation. For that purpose we first restrict our analysis to "small" clones by defining a cut-off size up to which clones are considered. The cut-off is chosen as the average *maximal* clone size one would expect under the clonal dynamics observed in HGDs, and can be determined by extreme value theory (*8*). Assuming an exponential CSD, the expected maximum clone size is $z_{\max} = (\ln(N) + \gamma_e) \times \bar{z}$, where N is the number of clones, γ_e the Euler-Mascheroni constant, and $\bar{z}$ the mean clone size. This results in an expected maximum clone size of 147 at 42 days after induction and a maximum expected maximum size of 147 at 56 days after induction. We will thus use these numbers as cut-off for our analysis.

Considering only clones below this threshold (65 out of 98 at 42 days, and 25 out of 40 at 56 days after induction), the clonal data is matched well by the prediction from model **17** with the parameters inferred for HGD clonal dynamics, *without Kras*, as shown in Fig. 8g at 42 days after induction and in Supplementary Fig. 7c at 56 days after induction. Hence, for the majority of clones, Kras induction does not have a significant impact on clonal dynamics.

However, there is still a large fraction of clones which are significantly larger than would be expected from dynamics in pre-malignant HGD. We want to test if these clones can yet be described by the tilted stochastic fate paradigm, rules **17**, albeit with a higher cell fate bias. Although we cannot fit the data, we can use an analytical approximation for the model prediction: after long times the clone size distribution approaches a distribution as expected from a super-critical branching process, which yields an exponential distribution $P(z) = 1/\bar{z} \exp(-z/\bar{z})$, where $\bar{z}$ is the mean clone size (*7*). Thus, the model rules **17** would predict the data points to collapse on the exponential curve when clone sizes are rescaled by the mean clone size. If the invasive super-large clones are excluded, the mean clone size $\bar{z}$ is 499 cells per clone after 42 days

and 560 cells per clone after 56 days. The resulting rescaled clone size distributions are shown in Fig. 8h and Supplementary Fig. 7d respectively (binned in intervals of 100, starting with size 150 for 42 days and with size 200 for 56 days after induction). Note that due to the lower cut-off c at $z = 150, 200$, the theoretical prediction is re-normalised by the normalisation factor $\mathcal{N} = (\sum_{i=\lceil c/100 \rceil}^{\infty} \exp(-100\, i/\bar{z}))^{-1}$, so that the theoretical prediction is $P(z) = \mathcal{N} \exp(-X)$, where $X = z/\bar{z} - 50$ (the function is shifted by half a binning interval to be evaluated in the middle of the interval). This shows an excellent agreement between theoretical prediction and the rescaled data. Thus we can conclude that the vast majority of clones in the invasive tumours is consistent with the tilted stochastic cell fate paradigm.

From this data are excluded the 'mega-clones' with several thousands of cells which do not match the predicted distributions. Although it could be possible that an even higher cell fate bias can accommodate for their size, the number of those clones is too small to test this.

References and Notes

1. D. P. Doupé, *et al.*, *Science* **337**, 1091 (2012).

2. E. Clayton, *et al.*, *Nature* **446**, 185 (2007).

3. B. D. Simons, H. Clevers, *Cell* **145**, 851 (2011).

4. D. T. Gillespie, *J. Phys. Chem.* **81**, 2340 (1977).

5. M. P. Alcolea, *et al.*, *Nature Cell Biology* **16**, 615 (2014).

6. E. R. Burns, L. E. Scheving, D. F. Fawcett, W. M. Gibbs, R. E. Galatzan, *The Anatomical Record* **184**, 265 (1976).

7. P. Haccou, P. Jagers, V. A. Vatutin, *Branching Processes* (Cambridge University Press, New York, 2005).

8. D. Sornette, *Critical Phenomena in Natural Sciences: Chaos, Fractals, Selforganization and Disorder* (Springer, Berlin, 2006).